



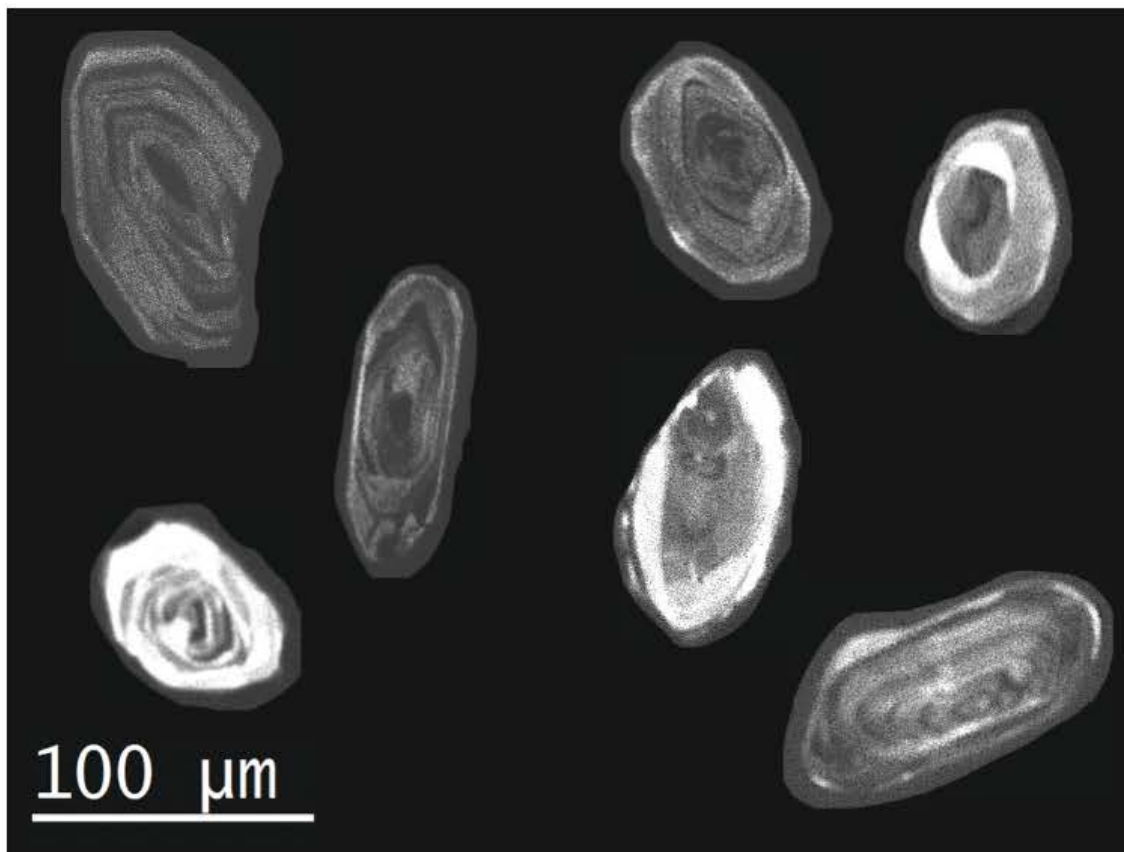
Stockholm
University

Bachelor Thesis

Degree Project in
Geology 15 hp

Zircon U-Pb Geochronology of the Bourne Complex, Ellesmere Island (Canada)

Filippa Carlson



Stockholm 2025

Department of Geological Sciences
Stockholm University
SE-106 91 Stockholm

Abstract

The Bourne Complex, located in northwestern Ellesmere Island, Canada, has an uncertain age and tectonomagmatic evolution. The complex consists of greenschist-facies, mafic, volcanic, and plutonic rocks, interbedded with tuffaceous and sedimentary units. Previous dating of the complex is based on limited $^{40}\text{Ar}/^{39}\text{Ar}$ data, which have yielded two widely different ages of 380 ± 10 Ma and 440 ± 2 Ma. It remains unclear whether the Bourne Complex is correlated with the magmatic rocks of the accreted Pearya terrane, the Svartevaeg Formation on the adjacent Axel Heiberg Island, or the volcanic rocks from Mount Rawlinson. The relationship between the Bourne Complex and these regional units is a focus of ongoing research. This study aims to better constrain the age of the Bourne Complex by using U-Pb geochronology of detrital zircons from a tuffaceous sample and evaluate it in the context of the regional geology. Petrographic investigations and Scanning Electron Microscopy (SEM) with Cathodoluminescence imaging guided the selection of zircons for subsequent U-Pb dating using Secondary Ion Mass Spectrometry (SIMS). The data revealed a detrital suite with distinct Neoproterozoic and Paleoproterozoic age peaks, indicating that the Bourne Complex has incorporated older crustal components, potentially from the Canadian basement. The two youngest analyses define a Maximum Age of Deposition (MAD) of 584 ± 11 Ma, which should be viewed as tentative until additional detrital zircons are analyzed. The data also reveal a Discordant lower intercept of 550 ± 36 Ma, interpreted as post-depositional lead loss caused by radiation damage from uranium-rich domains rather than a uniform alteration event. The tentative MAD is significantly older than existing argon ages and much of the surrounding sedimentary units on northwestern Ellesmere Island. However, it exhibits an overlap with Late Ediacaran metasediments from the Pearya terrane (Secession II) and the earliest phase of continental rifting along the Franklinian margin. To evaluate possible tectonomagmatic connections, zircons from a volcanic sample of the Svartevaeg Formation were also analyzed, yielding a U-Pb age of 431 ± 1.6 Ma. This is consistent with Silurian regional arc-related magmatism. A direct correlation between the Bourne Complex and the Svartevaeg Formation cannot be confirmed. However, their structural proximity could suggest a possible shared tectonomagmatic evolution associated with post-accretionary processes.

Keywords: Zircon geochronology, U-Pb dating, SIMS, Bourne Complex, Svartevaeg Formation, Pearya Terrane, Detrital zircon, MAD.

Table of Contents

1. Introduction.....	4
2. Geological setting.....	5
2.1 Northern Ellesmere Island.....	5
2.2 Bourne Complex.....	8
2.2.1 Previous age datings of the Bourne Complex.....	9
3. Theoretical framework.....	11
3.1 Uranium-Lead (U-Pb) geochronology.....	11
3.2 Zircon as a geochronometer.....	14
3.2.1 Textures in zircon.....	15
4. Methods.....	18
4.1 Sample collection and preparation.....	18
4.2 Thin section and hand sample petrography.....	19
4.3 SEM + CL imaging.....	20
4.4 SIMS U-Pb dating.....	21
4.4.1 The sample size determination.....	22
4.4.2 Data reduction.....	23
5. Results.....	24
5.1 Petrography.....	24
5.1.1 Petrographic overview.....	24
5.1.2 Summary Petrographic Table.....	25
5.1.3 Representative micro photos.....	26
5.2 Zircon textures and geochronology.....	27
5.2.1 Svartevaeg Formation geochronology.....	27
5.2.2 Bourne Complex geochronology.....	29
6. Discussion.....	32
6.1 Textural evidence for disequilibrium and open-system behavior.....	32
6.1.1 Mineral textures in Svartevaeg Formation.....	32
6.1.1 Mineral textures in Bourne Complex.....	33
6.2 Data reliability and age estimates.....	34
6.2.1 MAD evaluation.....	34
6.2.2 Older age populations and provinces.....	39
6.2.3 Timing of U-Pb disturbance.....	39
6.3 Regional tectonomagmatic constraints.....	41
7. Conclusions.....	45
7.1 Implications and future work.....	46
Acknowledgments.....	46
Appendix A - Mineral Abbreviations.....	51
Appendix B: Petrographic descriptions.....	51
VP17-26b.....	51
VP17-27.....	52

VP17-29.....	53
VP17-30.....	54
VP17-34.....	55
VP17-38.....	56
VP17-45.....	58
VP17-56.....	59
VP17-66.....	60

1. Introduction

Ellesmere Island is located in the northernmost part of the Arctic Canadian Archipelago, stretching from Baffin Bay in the south to the Arctic Ocean in the North (Figure 1). It is bounded to the east by the Nares Strait, which separates it from Greenland, and to the southwest by Nansen Strait, which separates it from Axel Heiberg Island. It is a vital area for understanding the tectonic and depositional record of the northern margin of Laurentia, as the region has experienced repeated cycles of continental rifting, magmatism, collision, and terrane accretion over the past one billion years, all of which have created complex tectonomagmatic relationships in the geological record. (Koch et al., 2024; Powell & Schneider, 2022; Estrada et al., 2003)

One of the less well-understood units in the area is the Bourne Complex, located in the northwestern part of Ellesmere Island, northwest of the Kleybolte Fault zone. It comprises a hybrid lithology of greenschist-facies mafic igneous and sedimentary rocks that differ from the sedimentary strata across the fault zone (Powell & Schneider, 2022). It has an unresolved origin and relationship to the regional geology (Trettin, 1998). Previous geochronological studies of the Bourne Complex have yielded two widely differing ages: a younger $^{40}\text{Ar}/^{39}\text{Ar}$ age of 380 ± 10 Ma (Henry, 1991) and a significantly older $^{40}\text{Ar}/^{39}\text{Ar}$ age of $439 \pm$ Ma (Powell & Schneider, 2022). The later age suggests a relationship with the Pearya terrane, a continental fragment potentially exotic to Laurentia, which was accreted onto the Laurentian margin in a succession of episodes spanning from the Ordovician to the Late Silurian (Powell & Schneider, 2022). However, the Ar isotope system may preserve the cooling age through closure temperature, rather than the crystallization age, and it is furthermore susceptible to resetting and prone to argon loss in the case of reheating of the system (White, 2015). Trettin (1996) suggested that the Bourne Complex could correlate with the Svartevaeg formation on the adjacent Axel Heiberg Island due to similarities in lithology and its structural proximity. Due to these uncertainties of the protolith ages, the Bourne Complex is only constrained to be pre-Devonian in age (Trettin, 1998). A more robust dating of the complex is necessary to place it within a larger geological context.

This study aims to investigate the uncertainties associated with the age of the Bourne Complex by using U-Pb zircon geochronology. Specifically, the study will:

1. Investigate the Maximum Age of Deposition (MAD) and potential older populations of a tuffaceous sample from the Bourne Complex.
2. Evaluate the age of the Svartevaeg Formation in the context of the regional geology, as it may share the same tectonomagmatic evolution as the Bourne Complex.

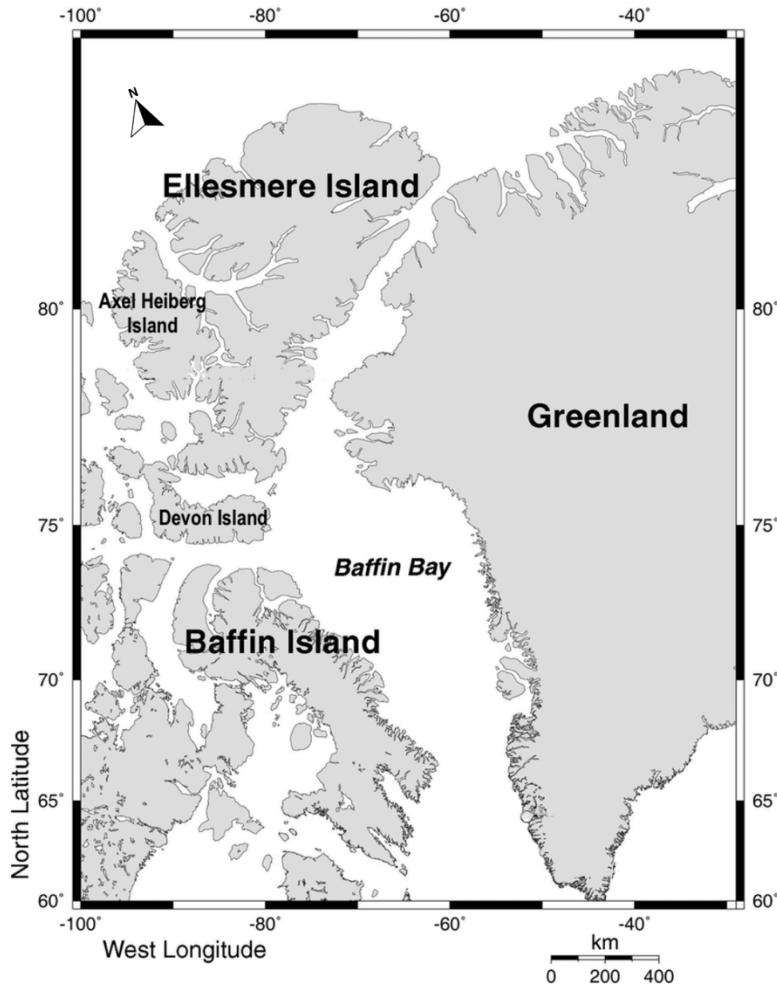


Figure 1: Map of Ellesmere Island and the adjacent Arctic Archipelago Islands. Map modified from Smol & Douglas (2007) (Figure 1).

2. Geological setting

2.1 Northern Ellesmere Island

Northern Ellesmere Island has a complex Early Paleozoic tectonic history, recording the transition from an Ordovician intra-oceanic magmatic arc system to Silurian strike-slip faulting, followed by Devonian collisional tectonics. The region records two main orogenic episodes. First, the Paleozoic Ellesmerian orogeny occurred when the Pearya terrane and other fragments collided onto the Franklinian margin of the Laurentian craton, producing widespread deformation and high-grade metamorphism across northern Ellesmere Island. Later, the Paleogene Eurekan orogeny occurred, an intraplate compressional event tied to the

opening of Baffin Bay, which reactivated older faults and generated intense, localized crustal shortening in central Ellesmere. (Koch et al., 2024; Faehnrich et al., 2023; Powel & Schneider, 2022; Schiffer et al., 2016)

The region is broadly divided into four major tectonic units (Figure 2), including the Canadian Shield, the Franklin Basin, the Sverdrup Basin, and the Pearya Terrane (Estrada et al., 2003). The Canadian Shield comprises the southeastern region and is primarily composed of an Archean basement of metavolcanic rocks overlain by Proterozoic metasediments and volcanics (Trettin, 1998). The basement is metamorphosed up to granulite facies (Estrada et al., 2003). The Franklinian Basin is Neoproterozoic to Devonian sedimentary basin located along the northern margin of Laurentia. It comprises a succession of clastic and carbonate rocks that show a transition from a coastal shelf environment in the southeast to a deep marine deposit characterized by turbidites and volcanic rocks in the northwest (Estrada et al., 2003; Trettin, 1998). The volcanic units include the Hazen Formation, the Kulutingwak Formation, and the Mount Rawlinson Complex, where the latter exposes Late Ordovician to Silurian arc-related volcanics and sills that intrude the Hazen Formation (Powell & Schneider, 2022). During the Ellesmerian orogeny, parts of the Franklinian basin were deformed into fold-and-thrust belts such as the Clements Markham Fold Belt, which forms a central province between Pearya to the north and the Franklinian shelf to the south (Estrada et al., 2003). The Sverdrup Basin is a post-Ellesmerian orogenic basin that unconformably overlies the deformed rocks of the Franklinian Basin and Pearya terrane (Estrada et al., 2003; Trettin, 1998). It comprises the central and western parts of northern Ellesmere Island and extends westward across Axel Heiberg Island into the offshore region. It consists of a thick, classic and organic sequence of deltaic, marine, and coal-bearing rocks (Estrada et al., 2003; Trettin, 1998). It subsequently underwent thermal subsidence and uplift from the Carboniferous to the Paleocene, and its later successions were locally removed in northern Ellesmere Island during later Eurekan deformation (Powell & Schneider, 2022).

The Pearya Terrane makes up the northernmost part of Ellesmere Island. It is interpreted either as an allochthonous Caledonian fragment, displaced and accreted onto the Laurentian margin during Paleozoic plate convergence, or as a pericratonic block that rifted from Laurentia and was later re-accreted during the Ordovician M'Clintock Orogeny (475-450 Ma) (Koch et al., 2022). It consists of Tonian basement rocks (960-980 Ma) and Neoproterozoic to Cambrian metasediments intruded by Ordovician arc-related plutonic and

volcanic rocks (469-481 Ma) (Koch et al., 2024). These units formed part of a subduction-related arc that was later accreted to Laurentia in a succession spanning from the Ordovician to the Late Silurian. Continued strike-slip motion in the Silurian deformed and altered the terrane, and units such as the Danish River Formation developed along the Pearya-Franklinian margin (Koch et al., 2022). Later, Ellesmerian and Eureka deformation caused multiple deformation events and metamorphic overprinting, which shaped the current structural boundaries between Pearya, the Franklinian Basin, and adjacent volcanic complexes (Koch et al., 2024; Powell & Schneider, 2022).

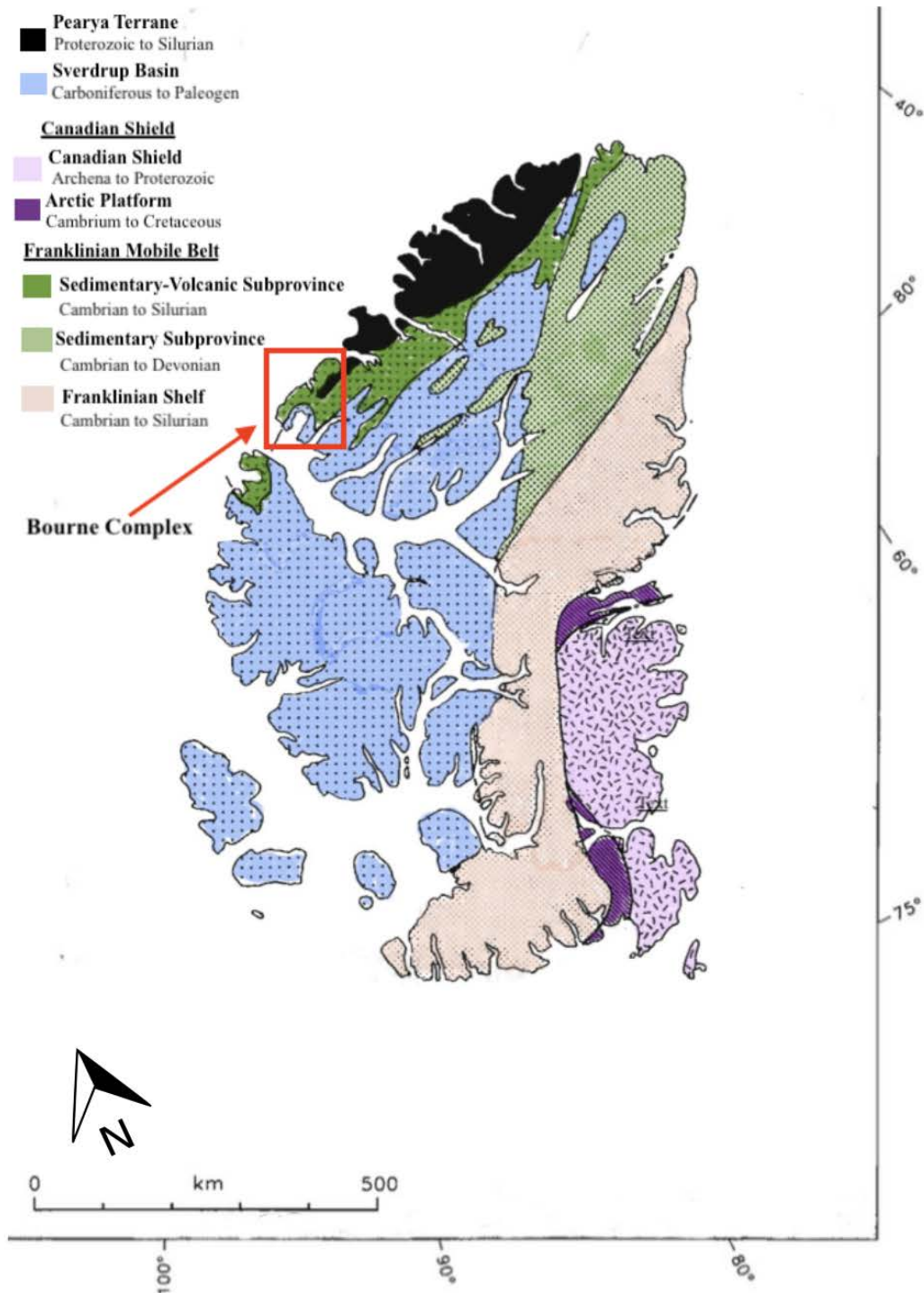
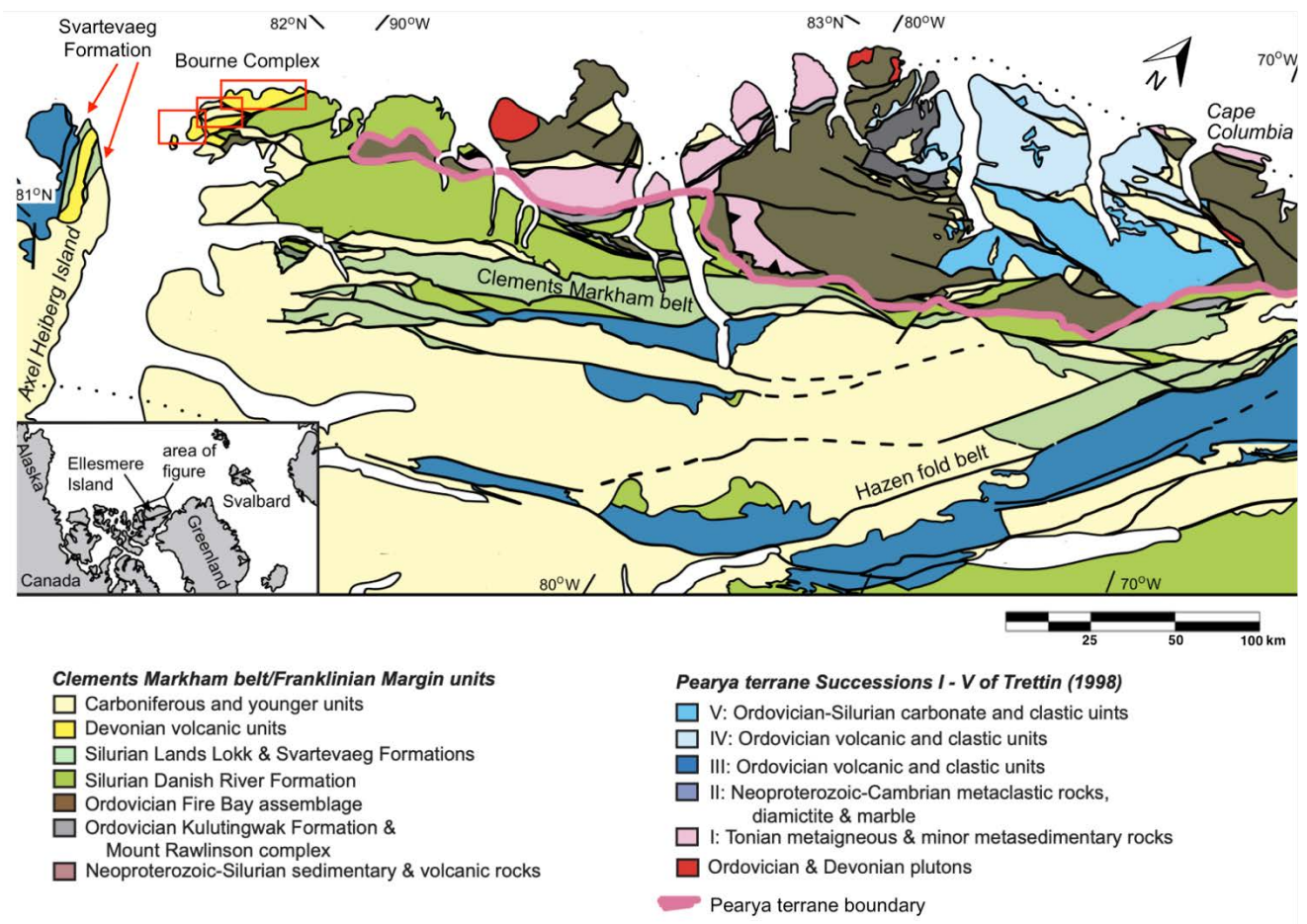


Figure 2: Map showing the four major tectonic units of the northwestern Ellesmere Islands. The study area (Bourne Complex) is indicated on the map as well. The map is modified from Trettin (1994) (Figure 4).

2.2 Bourne Complex

The Bourne Complex is composed of greenschist-facies mafic volcanic and plutonic rocks, with tuffaceous and sedimentary interbeds (Trettin, 1998). It is predominantly exposed along the Kleybolte Peninsula, with smaller exposures on Fjeldholmen and Kruger Islands (Figure 3). The complex is bounded to the southeast by the Kleybolte Fault Zone, which separates it

from the Silurian Danish River Formation. This fault zone also hosts the Imina Formation, composed of serpentized ultramafic rocks, including dunites of Late Ordovician to Early Silurian age (Trettin, 1996). The complex is relatively unstudied, partly due to poor exposures, difficulty of access, and complex structural relationships, such as an abundance of later intruding dikes and sills (Trettin, 1998). A study by Henry (1991) on the Fjeldholmen and Kruger islands provided a detailed investigation of the geochemistry of the Bourne Complex on these islands. He identified three main lithological groups: porphyritic andesite dykes, plagioclase porphyritic dykes, and North-trending basaltic dykes; the latter is not



considered part of the Bourne formation and is instead related to younger Arctic magmatism (Henry, 1991).

Figure 3: Geological map showing the proximity of the Bourne Complex and Svartevaeg Formation. The Bourne Complex is represented by its volcanic units. The map is modified from Koch et al. (2024) (Figure 1).

2.2.1 Previous age datings of the Bourne Complex

Dating of a porphyritic andesite from Fjeldholmen (Henry, 1991) yielded a $^{40}\text{Ar}/^{39}\text{Ar}$ age from primary hornblende of 380 ± 10 Ma, which was interpreted to represent the time of crystallization. However, the data showed large age dispersion, suggesting a complex thermal

history. The argon ratios were later suggested to have been affected by argon loss due to the intrusion of later dykes (Trettin, 1998). The Bourne complex can therefore potentially be older. A later $^{40}\text{Ar}/^{39}\text{Ar}$ isotopic study by Powell and Schneider (2022) based on the total fusion of seven muscovite grains from a volcanoclastic section of the Bourne Complex near the Kleybolte fault zone yielded an age of 439 ± 2 Ma. These authors suggested that it formed during or shortly after the accretion of Pearya, potentially as part of the post-M'Clintock volcanic arc activity. This hypothesis is strengthened by the fact that the Bourne region is lithologically different from the typical Franklin Basin sediments (Powell & Schneider, 2022). However, total-fusion $^{40}\text{Ar}/^{39}\text{Ar}$ ages can be misleading, as it may average inherited or excess ^{40}Ar and partial argon loss, resulting in anomalously old or young ages (Kelley, 2002)

Due to its structural position and lithological similarities, Trettin (1996) suggested that the Bourne may be correlative with the Svartevaeg Formation, located on the nearby Axel Heiberg Island. The Svartevaeg Formation is part of the Franklin succession. It is Lower Silurian in age, based on the discovery of graptolite fossils and a MAD of 428 ± 6 Ma from detrital zircons (Dewing et al., 2019). It consists of a lower volcanic unit (Member A), characterized by calc-alkaline andesites, basalt, and tuffs, with minor sedimentary and organic components (Hadlari & Madronich, 2017; Trettin, 1998). The upper unit (Member B) comprises volcanogenic sedimentary rocks, including mudstones, sandstones, siltstones, conglomerates, and volcanic tuff. Some of the older zircon grains match the Ordovician-Silurian ages typical of the Pearya terrane (Dewing et al., 2019), which reinforces a possible regional correlation of the arc magmatism across Northern Ellesmere Island.

Both the Bourne and Svartevaeg lie in the tectonic corridor between Pearya and the Franklinian Basin and could record different stages of arc-related volcanism and basin development. Therefore, the Bourne Complex is crucial for understanding the early tectonic development of the area, underscoring the need for further isotopic studies to refine the understanding of the area's geological evolution.

3. Theoretical framework

3.1 Uranium-Lead (U-Pb) geochronology

The U-Pb isotopic system is widely used in geochronology, particularly for dating minerals such as zircon, monazite, and titanite (Schaltegger et al., 2015). The system involves the radioactive decay of uranium and/or thorium isotopes into lead isotopes, with three main decay chains: $^{238}\text{U} \rightarrow ^{206}\text{Pb}$, $^{235}\text{U} \rightarrow ^{207}\text{Pb}$, and $^{232}\text{Th} \rightarrow ^{208}\text{Pb}$ (Schoene, 2014). Each chain involves a series of alpha and beta decays, creating intermediate daughter isotopes that eventually decay into the stable lead isotopes of their respective parent. The lead isotopes accumulate over time in a predictable manner, following a timeline described by the half-lives of the parent isotopes and their decay constants (Table 1).

Table 1: The U-(Th)-Pb isotopic system showing the parent isotope and its resulting isotopic daughter product. The half-life and decay constant (λ) are obtained from Schoene (2014).

Parent	Daughter	Half-life (yr)	λ (yr^{-1})
^{238}U	^{206}Pb	$4.468 * 10^9$	$1.55125 * 10^{-10}$
^{235}U	^{207}Pb	$703.8 * 10^6$	$9.8485 * 10^{-10}$
^{232}Th	^{208}Pb	$14.05 * 10^9$	$4.9475 * 10^{-11}$

The decay process and the radioactive growth of the daughter isotopes (D) over time (t) is mathematically described by the simplified exponential-decay law (equation 1), where P_0 represents the amount of parent isotopes present at t_0 (mineral formation) and λ is the isotope-specific decay constant (White, 2015).

$$D = P_0(1 - e^{-\lambda t}) \quad (1)$$

In U-Pb geochronology, each decay system can be used to investigate the radiometric age of a sample. However, because open-system processes, such as magma mixing or contamination, can disrupt and/or reset the isotopic ratios, the age data must be evaluated for concordance (Ireland & Williams, 2003). This highlights one of the greatest strengths of the U-Pb system: its dual decay of uranium (^{238}U and ^{235}U), which enables cross-validation and two independent age determinations. If the system has remained closed, these ratios should yield consistent and concordant ages (Williams, 1998). The concordant data points plot along

a defined curve, known as the Concordia, on a Wetherill diagram where the x-axis represents the $^{206}\text{Pb}/^{238}\text{U}$ ratio, and the y-axis represents the $^{207}\text{Pb}/^{235}\text{U}$ ratio. Data points that deviate from this curve are considered discordant and are indicative of open-system behavior which can result in lead loss or lead gain (Schoene, 2014). If the data shows discordance, a Discordia line may be fitted through the data, with the upper intercept indicating the true crystallization age of the samples and the lower intercept representing the timing of disturbance that causes the lead loss (Schoene, 2014). The Wetherill diagram is useful for comparing multiple U-Pb ages from a sample and interpreting data for older samples (>1200 Ma) (Ireland & Williams, 2003). An alternative method for analyzing concordance is the Tera-Wasserburg diagram, where the parent-daughter ratio ($^{238}\text{U}/^{206}\text{Pb}$) is plotted against the isotopic composition of lead ($^{207}\text{Pb}/^{206}\text{Pb}$). This method is useful for analyzing data that may be affected by common lead, as it identifies mixing trends between radiogenic and initial lead compositions (Williams, 1998).

The age of a sample is then calculated by measuring the ratio of radiogenic lead to its parent isotope, and with knowledge of its half-life, these ratios are used in age equations derived from the radioactive decay laws (Schoene, 2014). When the U-Pb data plot along the Concordia curve, indicating negligible open-system behavior, a single concordant age can be calculated directly from the parent-to-daughter ratio using the standard decay equation (Equation 2)

$$\begin{aligned}
 {}^{206}\text{Pb} &= {}^{238}\text{U} * (e^{\lambda 238t} - 1) \\
 {}^{207}\text{Pb} &= {}^{235}\text{U} * (e^{\lambda 235t} - 1) \\
 {}^{208}\text{Pb} &= {}^{232}\text{Th} * (e^{\lambda 232t} - 1)
 \end{aligned} \tag{2}$$

The age is determined by solving these equations for t, which represents the time since the mineral formed. The equations hold under a set of conditions, including: (1) the mineral has formed in a closed system, (2) the decay chains are in secular equilibrium so that the number of parent isotopes decaying to their specific daughter isotope is balanced by the rate at which the daughter isotope is produced and (3) the $^{238}\text{U}/^{235}\text{U}$ ratio is fixed at 137.818. This last assumption enables conversion between different U-Pb systems without requiring direct measurement of both U isotopes. In the case of discordant data, the Discordia line in the

Wetherill or Tera-Wasserburg diagram can be used to investigate in the age of the sample. (Schoene, 2014; Ireland & Williams, 2003; Williams, 1998).

However, not all lead in a sample must be the result of radioactive decay. Common Pb is a general term referring to lead that originates from external sources and is unrelated to the radioactive decay of uranium and thorium. Initial Pb, on the other hand, is lead that was present at the time of zircon crystallization. Both types affect the isotopic ratios and, thus, the accuracy of the age calculations. For zircon, its initial Pb is typically assumed to be zero, and common Pb is often introduced through contamination during laboratory processing. ^{204}Pb is considered the primary form of common Pb since it is non-radiogenic and inherited from external sources, such as surrounding country rock or fluid interactions. Even ^{206}Pb and ^{207}Pb can be classified as common Pb if they are inherited from external contamination rather than the decay of uranium or thorium. (Schoene, 2014; Ireland & Williams, 2003; Williams, 1998).

To correct for common Pb in U-Pb zircon geochronology, the Stacey & Kramer's model (1975) is typically used. This model predicts the isotopic composition of common Pb at any given time in Earth's history and provides age-dependent values for the $^{206}\text{Pb}/^{204}\text{Pb}$, $^{207}\text{Pb}/^{204}\text{Pb}$, and $^{208}\text{Pb}/^{204}\text{Pb}$ ratios, representing the Pb "background" inherited from the mantle/crustal reservoirs prior to zircon crystallization. This common Pb component is then subtracted from the total Pb measured in the sample to ensure that only radiogenic Pb derived from U/Th decay is used in the age calculations (Schoene, 2014; Williams, 1998). For younger zircons (<1200 Ma), a common Pb correction may be necessary. Young zircons have not had sufficient time to accumulate radiogenic Pb, and common or inherited Pb becomes more significant; therefore, these ratios are more sensitive to common Pb (Williams, 1998). For older zircons (>1200 Ma), a correction may or may not be necessary, depending on whether the isotopic ratios indicate an isolated closed system that lacks contamination or not.

Lastly, in detrital zircon populations, the age derived from the $^{206}\text{Pb}/^{238}\text{U}$ ratio is often reported for younger grains (< 1200 Ma) due to the significantly longer half-life of ^{238}U (Ireland & Williams, 2003). For older zircon grains (>1200 Ma), the age derived from the $^{207}\text{Pb}/^{206}\text{Pb}$ ratio is typically used. The decay of ^{235}U to ^{207}Pb has a significantly shorter half-life; therefore, the decay progresses more rapidly, resulting in greater lead accumulation, making it less sensitive to common Pb, and yielding a more precise and robust age (Ireland & Williams, 2003).

3.2 Zircon as a geochronometer

Zircon, $ZrSiO_4$, is considered a robust geochronometer and occurs naturally in various geological environments, including igneous, metamorphic, sedimentary, and hydrothermal systems (Pupin, 2024). One of the advantages of zircon is that it incorporates uranium and thorium during crystallization while excluding lead (Ireland & Williams, 2003). Therefore, most of the lead found in zircon is produced by the radioactive decay of uranium and/or Thorium. A further benefit of zircon is its chemical and physical durability, as well as its capacity to retain complex growth histories over geologic time (Ireland & Williams, 2003). It has a high closure temperature (often exceeding $900^{\circ}C$), enabling it to survive high-grade metamorphism, erosion, and other processes that usually otherwise reset or destroy the geological record (Ireland & Williams, 2003; Corfu et al., 2003). Zircon can thereby record multiple crystallization events within a single grain and preserve distinct growth domains that can be dated separately (Corfu et al., 2003).

The formation of zircon is influenced by various factors, including temperature, pressure, and the presence of fluids (Pupin, 2024). An accurate classification of the grain's origin is crucial for further analysis, as an obtained radiometric age corresponds to different growth events, such as either the timing of primary crystallization or a metamorphic recrystallization event (Corfu et al., 2003).

The formation of zircon in igneous systems is primarily controlled by the zirconium (Zr) saturation of the melt (Corfu et al., 2003). Zircon typically crystallizes from a melt as part of the early crystallization sequence due to its incompatibility when the melt becomes saturated with respect to Zr (Pupin, 2024). In some cases, zircon can continue to crystallize throughout the cooling process, particularly in fluid-rich systems (Pupin, 2024; Corfu et al., 2003). The temperature of the magma also influences the crystallization of zircon. Higher temperatures typically favor the formation of more euhedral, well-developed zircon grains, while lower temperatures may lead to more irregular, resorbed zircon habits (Pupin, 2024).

In metamorphic systems, zircon can either form new grains from fluids or undergo recrystallization and chemical modification of pre-existing grains (Pupin, 2024). New growth often occurs during prograde metamorphism, when Zr can be released from other minerals, while at the same conditions preexisting zircons may undergo recrystallization, partial dissolution, and reprecipitation, especially in the presence of fluids (Pupin, 2024; Corfu et al.,

2003). Because zircon is resistant to diffusion under dry conditions, extensive alteration typically requires fluid activity, which can be from either aqueous or silicate melts, and higher temperatures and pressures (Zeng et al., 2022). Low-grade metamorphism in dry conditions generally does not impact zircon textures and growth (Pupin, 2024). Some metamorphic zircons may also retain relics of igneous growth, which are referred to as "ghost textures" (Corfu et al., 2003). Hydrothermal zircon typically forms during metasomatism, often as a secondary product from rock-fluid interactions (Zheng et al., 2022). These zircons often exhibit distinct features, such as enrichments in the light rare earth elements (LREEs), dissolution textures, or inclusion-rich rims (Pupin, 2024; Zheng et al., 2022).

Zircons in sedimentary systems are typically detrital, representing eroded and reworked metamorphic or igneous grains that have been incorporated and lithified during sedimentation (Pupin, 2024). Detrital zircon dating yields mixed-aged populations, especially if the sedimentary unit has incorporated zircon grains from different origins, and a coherent, concordant age is not usually obtained from detrital populations (Sharman & Malkowski, 2020). In these cases, a MAD can be used as a proxy for the true depositional age, provided that rapid sedimentation, exhumation, and transport are assumed (Cawood et al., 2012). A sedimentary unit cannot be older than the youngest analyzed grain contained within it. Some conservative methods, such as using the weighted mean of multiple overlapping young grain ages, yield a more reliable MAD (Sharman & Malkowski, 2020). This approach reduces the risk of bias from lead loss, analytical scatter, or contamination, and it provides a more robust age constraint than relying solely on the youngest grain. Dating of detrital grains can also show indicative peaks of several grains, indicating a common source for the sedimentary unit (Sharman & Malkowski, 2020).

3.2.1 Textures in zircon

Zircon can exhibit a wide range of textures, providing insights into its geological history (Figure 4). Due to its high resistance to alteration, these textures can be preserved in detail and observed through various imaging techniques such as cathodoluminescence (CL) or backscattered electron imaging (BSE) (Pupin, 2024; Corfu et al., 2003).

Igneous zircons typically display elongated and prismatic shapes. Additionally, they often exhibit growth zonation, allowing for the distinction of individual growth events. One of the most characteristic zonation's is oscillatory zoning, characterized by alternating bands of different compositions that reflect cyclic variations in the magma's chemical composition

during crystal growth. Well-developed, undisturbed oscillatory zoning often indicates that zircon growth has occurred in a relatively stable and closed system. In contrast, resorbed or skeletal textures and truncated zoning indicate disruption and open system behaviors, likely caused by magma mixing or contamination by country rock. Another type of zonation pattern is sector zoning, which occurs when different crystallographic sectors of the zircon grow at different rates. This often also reflects changes in the melt's chemical composition, and it is common for crystals that grow in a homogeneous melt, where variations in temperature or chemistry are subtle but continuous. Sector zoning can be linked to the gradual differentiation of a magma chamber and is often observed in large zircon crystals in plutonic rocks. (Pupin, 2024; Corfu et al., 2003).

Zircons that have undergone metamorphism typically exhibit more rounded or multifaceted morphologies, reflecting the alteration of their original crystal shape. A common metamorphic feature is the development of zircon overgrowths, where new zircon recrystallizes on pre-existing cores. These overgrowths generally exhibit compositional differences from the core as they form from chemically distinct melts or fluids.

Recrystallization can also often preserve remnants of earlier domains as ghost textures within newly formed zircon domains. Patchy zoning often develops in response to partial recrystallization, indicative of re-equilibration processes such as diffusion and rock-fluid interactions. More extensive recrystallization can alter the zircon shape, size, and internal structure, producing domains with distinct compositions and textures. These changes are often driven by high-temperature metamorphism or interactions with hydrothermal fluids. Under such conditions, zircon can incorporate or redistribute trace elements such as U, Th, and REEs, particularly along altered domains or fractures. Hydrothermal alteration may further enhance this process, forming U-rich rims or spongy and porous textures. Some hydrothermal zircons specifically grow as thin films around other minerals such as rutile or ilmenite. (Pupin, 2024; Zheng et al., 2022; Corfu et al., 2003)

Zircon may undergo extensive resorption in high-grade metamorphic environments, resulting in irregular, cauliflower-like zonation patterns that are indicative of intense recrystallization (Pupin, 2024). Primary oscillatory zoning is often disturbed at high temperatures and replaced by homogeneous or sector-zoned domains (Corfu et al., 2003). In contrast, high-pressure conditions, equivalent to eclogite facies, commonly result in subrounded zircon morphologies with internally homogeneous textures (Corfu et al., 2003). In low-grade metamorphism,

resembling greenschist facies, zircon alteration is generally limited due to the mineral's high closure temperature. However, localized modifications may still occur along fractures and radiation-damaged zones, often resulting in botryoidal or feathery alteration fronts (Pupin, 2024; Zheng et al., 2022).

Additional textures that give important information are fractures and inclusions. Fractures can result from metamictization, a process of structural damage caused by the radioactive decay of uranium and thorium within the crystal (Pupin, 2024). Over time, the accumulation of radiation damage leads to volume expansion in particular uranium-rich zones that exert stress on the surrounding, less damaged regions. This differential expansion often results in internal fracturing of the zircon crystal (Corfu et al., 2003). These fractures commonly function as fluid pathways, promoting alteration, partial recrystallization, and element redistribution during metamorphic and hydrothermal events (Zheng et al., 2022). In CL imaging, the effects of metamictization and fluid-assisted alteration are observable as fuzzy or mosaic textures, particularly in domains adjacent to fractures or damaged zones (Zheng et al., 2022; Corfu et al., 2003).

Sedimentary and detrital zircons often show rounded, subangular, or fragmented shapes, which is a result of abrasion and rework during transport and sedimentation. Despite abrasion and erosion, detrital zircons often retain complex zoning patterns and internal textures that record their original igneous or metamorphic formation. (Pupin, 2024).

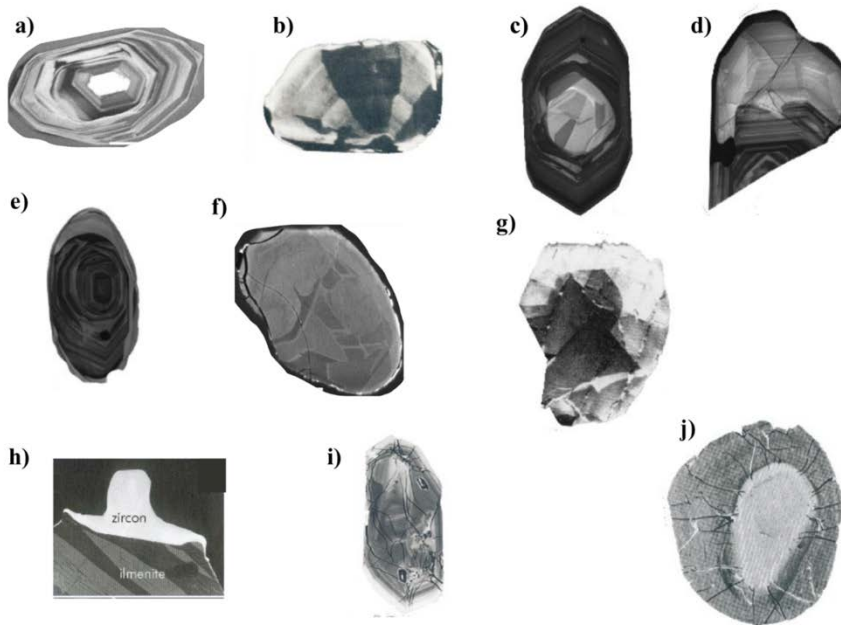


Figure 4: Different textures in zircons from Cathodoluminescence (CL) imaging. All images are approximately 70-250 μm . Figures 4a and 4f, are retrieved from Zheng et al. (2022). Figure 4. b-e and 4. g-j is retrieved from Corfu et al. (2003). a) Igneous zircon with oscillatory zoning, b) igneous zircon with sector zoning c) xenocryst core in igneous zircon surrounded by new igneous growth displaying faint oscillatory zoning, d) igneous zircon with a partially resorbed core, indicating reheating of the system, e) zircon with an zoned igneous core, with an metamorphic outer rim exhibiting a homogeneous texture, f) metamorphic zircon with distorted/chaotic texture indicative of high-grade alteration, g) subrounded metamorphic zircon with patchy zonation, h) hydrothermal alteration where zircon grown around ilmenite, i) fractured zircon with abundant U/Th rich inclusions, the fractures propagate from these inclusions, j) zircon with radial fractures from the other core to the rim, darker rim around the core suggest a high U/Th domain that caused the expansion and fracturing of the grain.

4. Methods

4.1 Sample collection and preparation

All samples were collected by Victoria Pease during the 2017 Circum-Arctic Structural Events 19 expedition to Ellesmere Island. They were sampled across the Kleybolte Peninsula and northern Axel Heiberg Island. This study analyzed mineral samples related to zircon occurrences in 10 thin sections and their corresponding hand sample. Pease then conducted mineral separation on selected samples (a total of seven samples) to extract single zircon grains for subsequent Scanning Electron Microscopy (SEM) and Secondary Ion Mass Spectrometry (SIMS) analysis. All mounts used for the SEM and SIMS were prepared by Kerstin Lindén at the National Museum of Natural History (NRM), Stockholm. The preparation procedures followed the epoxy-mount protocol explained by Ling et al. (2020) and are summarized below.

The samples were initially cleaned to remove oils and dust. The samples were then divided across two separate flat mounts, each with a diameter of 10 mm and a depth of 25 mm (Figure 5a–b). In addition, the zircon Geostandard (91500) was also placed in the top center of each mount for SIMS calibration. This was followed by epoxy fixation and degassing under a high vacuum to remove bubbles. The mounts were polished manually using diamond pastes, and the polishing continued until a topography of less than 3 μm remained. After final polishing, the mounts were rinsed with acetone and ethanol and oven dried. A thin gold conductive film was sputtered onto each mount before the SEM to mitigate the charging of the insulating zircon under the electron microscope.

From the SEM, two samples were identified as suited for subsequent U-Pb dating with SIMS, one from the Bourne complex and one from the Svartevaeg Formation. The same mounts were reused for U-Pb SIMS dating; however, before an additional, thicker gold film was applied, the ion probe used in the SIMS operated at a higher voltage than the SEM.

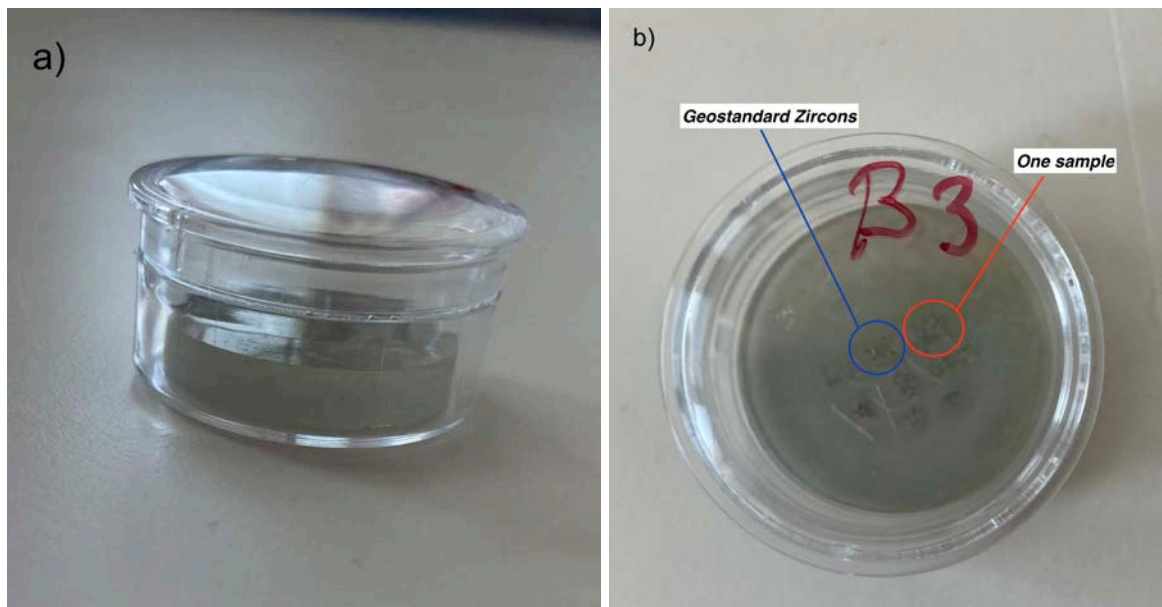


Figure 5: a) Sample mount used in the SEM showing thick epoxy base with thin gold coating, b) placement of samples and zircon Geostandard (91500) on the mount.

4.2 Thin section and hand sample petrography

Hand specimens were inspected with a 10x hand lens to record mineral composition and grain size. Thin-section microscopy was performed using a Leica DMLSP microscope. The samples were analyzed in cross-polarized light (XPL) and plane-polarized light (PPL). All thin sections were also scanned in PPL and XPL by a Nikon Super Coolscan 9000 ED with

the Nikon Scan 4.0.2 software to study mineral modal abundance. The goal of these petrographic analyses was to identify the modal abundance, textures indicative of open or closed systems, mineral relationships, and indications of alteration.

4.3 SEM + CL imaging

The SEM uses a focused beam of electrons, in contrast to the light source used for the thin section analyses. This enables a significantly higher resolution of a sample's surface morphology and element distribution (Kannan, 2018). The sample gets bombarded by high-energy electrons that scan it in a raster pattern. The interaction causes an energy exchange with the sample surface, resulting in the reflection of high-energy backscattered electrons (BSE), emission of low-energy secondary electrons (SE) and Auger electrons, and the emission of electromagnetic luminescence such as cathodoluminescence (CL). Different detectors on the SEM then detect and obtain the signal of these emissions (Corfu et al., 2003). SEs are emitted from the surface layer and are used to create detailed images of a zircon external morphology, including fractures and inclusions, while BSEs highlight contrasts in atomic number and are especially useful for identifying compositional zoning related to heavy elements such as Hf and U in zircon (Kannan, 2018; Corfu et al., 2003).

This study used SE and CL images together, a standard paired analysis, as these provide different and complementary insights into the zircon grains. CL imaging is particularly useful for studying the internal textures and growth patterns of the zircon (Corfu et al., 2003). The CL emission occurs when the high-energy electron beam excites the electrons in the mineral, causing them to emit visible light in the form of photons (Kannan, 2018). The intensity of luminescence is dependent on structural defects, variations in the crystal lattice, and the presence of trace elements, particularly the rare earth elements (REEs), such as Dy^{3+} , Sm^{3+} , Eu^{2+} , as well as U, Th, and Hf, in the case of zircon (Zheng et al., 2022). These elements can significantly impact the zircon CL signature, and the variations correspond to different growth and alteration events within the mineral (Corfu et al., 2003). The technique is useful as it helps to target specific zones for subsequent isotopic dating, ensuring that age analyses are tied to a single growth event (Ireland & Williams, 2003). The CL images are in greyscale, with the bright areas corresponding to areas with high concentrations of the emitted luminescent source elements. However, high concentrations of U^{4+} correspond to highly

metamictized areas that have experienced radiation damage, which suppresses the CL emission, and they will thereby appear darker in the images (Corfu et al., 2003).

The analysis was done using the FEI Quanta 650 FEG at the NRM (Figure. 6a-b). Both the SE and CL analyses were done under high vacuum, which is necessary for beam stability and signal clarity to prevent interference from air contamination (Kannan, 2018). The specific set-up conditions for the SEM were an accelerating high voltage of 15.0 kV and a chamber pressure of 0.10 mbar. The SE and CL imaging were conducted separately, one at a time. Once the imaging was complete, the images were printed out and analyzed to identify areas of interest for subsequent SIMS analysis, excluding areas with cracks, inclusions, and high uranium metamict domains. The ion microprobe used for the SIMS ranges from 10-25 μm , so the regions of interest had to be larger than that to reduce sources of error by analyzing cross-regional parts of possible different growth events or parts of the surrounding epoxy.

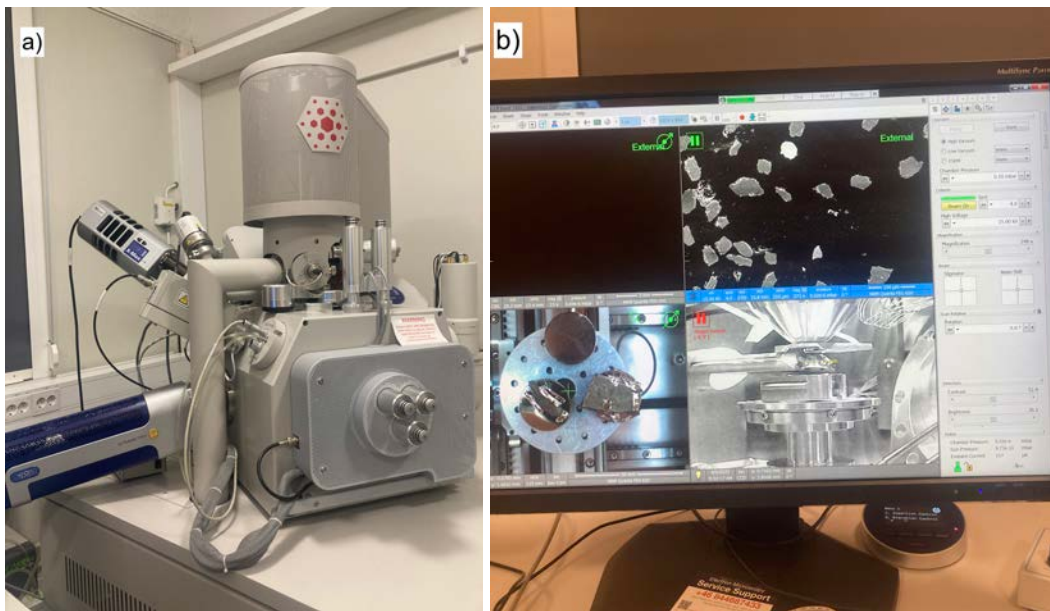


Figure 6: a) the SEM at NRM, b) the computer set up for the SEM showing the analysis with the SE view (top right corner).

4.4 SIMS U-Pb dating

SIMS is a type of mass spectrometer used to analyze a sample's chemical structure and measure the mass-to-charge ratio (m/z) of its isotopic composition. It focuses a high-energy primary ion beam of oxygen ions (O^{2-}) onto the sample, which causes the atoms in the sample to become charged (ionized) and ejected as secondary ions (and some neutrons) that reflect the chemical and isotopic composition of the sample. The secondary ions are then extracted and directed into a mass spectrometer for analysis, where they are measured by their m/z

ratio. The extraction method involves an accelerating process that applies an electromagnetic field to pull secondary ions from the sample surface and deflect them based on their m/z . Lighter ions are deflected more than heavier ones, and the resulting mass spectrum is used to calculate the relative abundances of various isotopes in the sample. (Schoene, 2014; Ireland & Williams, 2003; Williams, 1998).

The SIMS U-Pb analyses were performed at the NORDSIMS Laboratory at NRM using the Cameca IMS1280 (Figure 7). Whitehouse et al. (1999) and Whitehouse and Kamber (2005) describe the analytical procedures and setup conditions for the ion probe. The O^{2-} primary ion beam was focused to a spot size of 15 μm or 10 μm , depending on the size of the zircon crystal. The m/z values were calibrated relative to the Geostandard zircon 91500 reference, which has a known age of approximately 1065 Ma (Wiedenbeck et al., 1995). Common Pb corrections were calculated using modern common Pb composition based on Stacey & Kramer (1975), and ^{204}Pb was measured when the ^{204}Pb count rate was above the detection limit. Calculations and diagrams of the U-Pb SIMS data were produced using Isoplot 4.15 for Microsoft Excel (Ludwig, 2011)

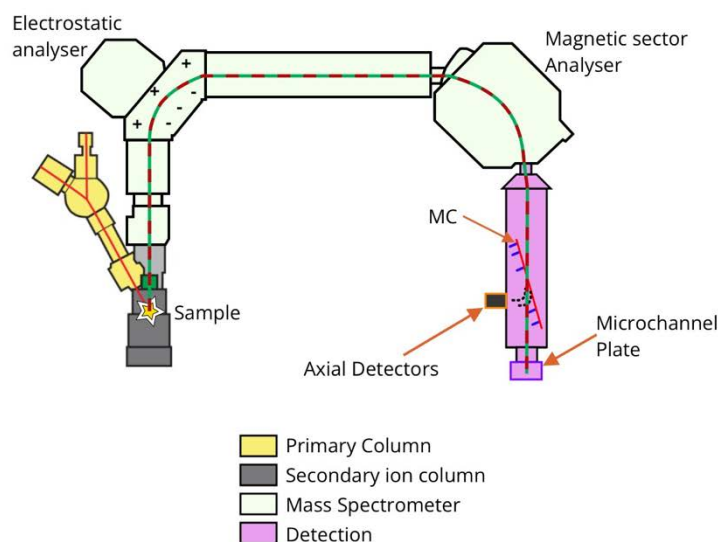


Figure 7: Schematic view from above of the SIMS Cameca IMS1280 ion probe. The figure is retrieved from Microscopy Australia, available at: https://myscope.training/SIMS_Common_features_of_the_Large_Geometry_and_NanoSIMS

4.4.1 The sample size determination

The sample size (n) for the SIMS was determined based on the type of sample that was going to be U-Pb analyzed. The goal for igneous zircon samples from a single-age population is to

obtain a robust crystallization age. High-precision data based on Chemical Abrasion-Thermal Ionization Mass Spectrometry (CA-TIMS) studies show that, once grains are demonstrably concordant, a weighted mean calculated from fewer than five single-grain analyses can already achieve a precision of ± 0.05 - 0.10 % across all decay chains (Schoene, 2014). To provide an internal check on subtle Pb-loss or inheritance, 10-20 spots per igneous sample that showed demonstrably concordance were analyzed, which is comfortably above the theoretical minimum while remaining analytically efficient.

Detrital samples require a different approach because the objective is to estimate a MAD from the youngest sub-population. Capturing rare young grains requires larger datasets; however, purely the “youngest-grain” algorithms drift systematically to spuriously young values as the sample size increases (Vermeesch, 2021). For the detrital samples in this study, the final count was based on 90 SIMS analytical spots. The MAD was calculated using a kernel density diagram which estimates the probability density of different age populations in a sample and then the *n*-grains mean method, where the age is defined by the weighted mean of the youngest concordant and statistically overlapping age clusters to guard against Pb loss or analytical outliers (Spencer et al., 2016).

4.4.2 Data reduction

The data were statistically evaluated using the Mean Square Weighted Deviation (MSWD) of the concordance and equivalence (C+E) with a 2σ confidence interval, described by Ludwig (2011). This value is based on how closely individual spots lie on the Concordia curve (C) and how consistent those spots are in sharing a single weighted-mean age (E), meaning how statistically consistent all analyses are with a single age population. A value close to 1.0 indicates that the data scatter is fully explained by the analytical uncertainties, and the analyses form a single, concordant population. A value much lower or higher indicates a poor fit that does not resemble concordance. The data were also evaluated in terms of the probability of C+E, which is the X^2 p-value for the same test. This value ranges from 0.0 to 1.0. Analyses with P-value ≥ 0.05 were considered statistically significant, while those with P-value < 0.05 were either rejected or further investigated for Pb loss, inheritance, or analytical problems.

5. Results

5.1 Petrography

The following section will display the petrographic observation made in hand sample and thin section. It is based on one sample from the Svartevaeg Formation (VP17-26b) and nine samples from the Bourne Complex (VP17-27, -29, -30, -34, -38, -44, -45, -56, -66).

5.1.1 Petrographic overview

VP17-26b is a mafic plagioclase-porphyritic rock in which subhedral to anhedral plagioclase phenocrysts (often exhibiting simple- and polysynthetic twinning, oscillatory zoning, and local embayment's) dominate alongside pseudomorphs of amphibole now replaced by fibrous chlorite and sparse opaque oxide grains. These phenocrysts are set in a brownish groundmass of fine plagioclase laths, chloritized amphibole, and opaques, reflecting low-temperature alteration. Minor calcite occurs as twinned, rhombohedral microphenocrysts and as fine-grained masses with oxide inclusions.

The Bourne samples comprise five medium-to coarse-grained mafic plutonic rocks of gabbroic composition (VP17-27, -30, -38, -44, -56), three volcanic equivalents (VP17-29, -34, -45), and one welded lithic-crystal tuffaceous rock (VP17-66). The plutonic rocks exhibit a framework of plagioclase and clinopyroxene, commonly with sericitized, embayed, and sieve-textured plagioclases as well as embayed clinopyroxene with chlorite alteration and thin actinolite reaction rims. The volcanic samples retain aphanitic to cryptocrystalline textures, some of which contain glass shards and flow banding. The tuffaceous rock consists of poorly sorted lath-shaped plagioclase, rounded quartz grains, and volcanic lithic fragments set in a devitrified, chlorite-rich matrix. All Bourne samples have a general composition of primary plagioclase, clinopyroxene, and opaque oxides, with varying occurrences of hornblende, biotite, and calcite. They also exhibit evidence of a secondary alteration phase characterized by sericitized and chloritized plagioclase, and the clinopyroxenes are variably replaced by chlorite, actinolite, and epidote.

Modal abundances, alteration assemblages, and key textures are summarized in Table 2 and illustrated in Figure 8. Mineral abbreviations and full petrographic descriptions are given in Appendices A and B.

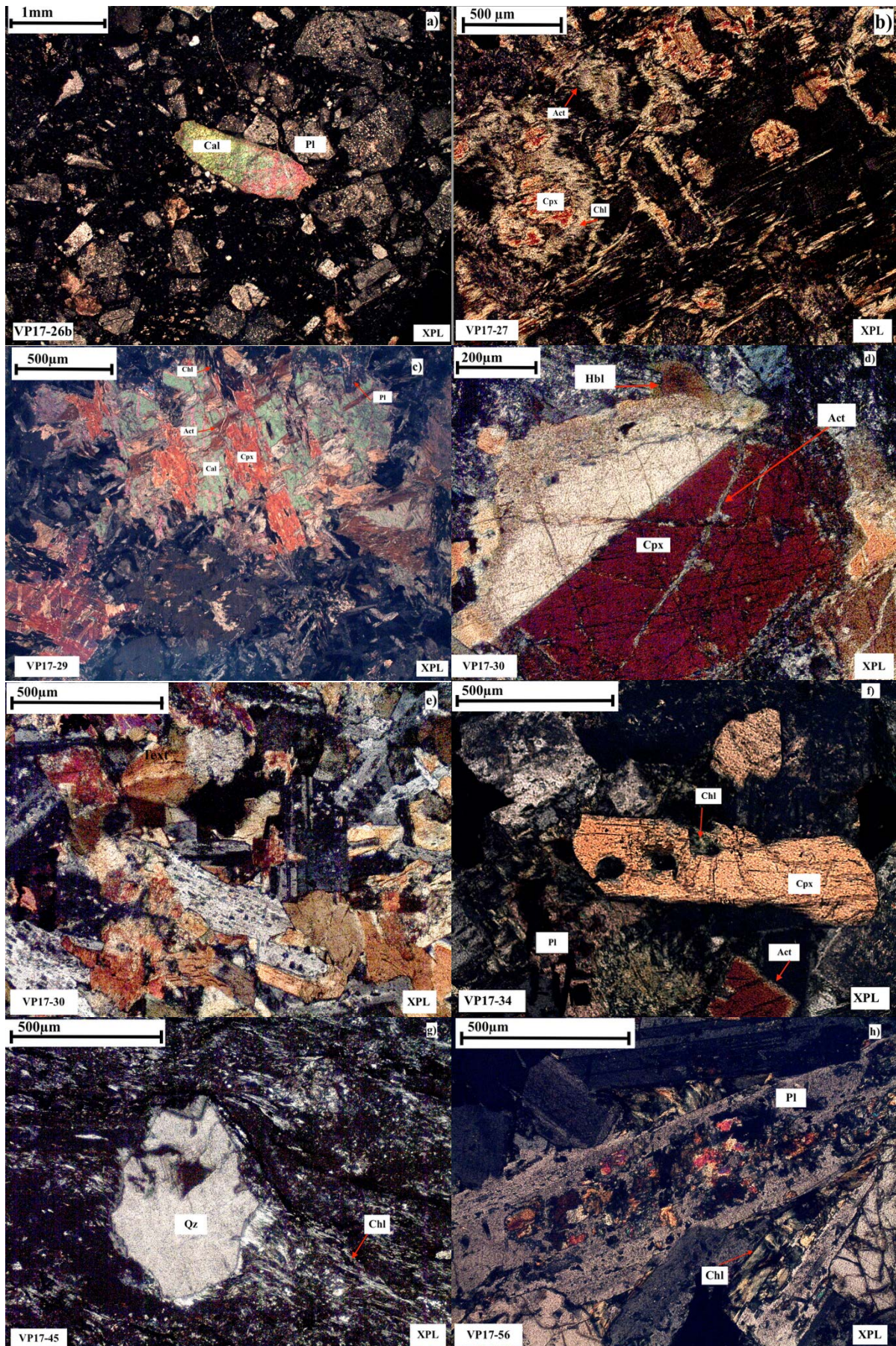
5.1.2 Summary Petrographic Table

Table 2: Summary of lithology, primary modal minerals, alteration assemblages, and diagnostic textures for the Svartevaeg and Bourne samples.

SAMPEL	LITHOLOGY	PRIMARY MINERALS	ALTERATION MINERALS	KEY TEXTURES
VP17-26B	Plagioclase-porphyritic rock	Pl (54%), Amp (6%), Opq (7%), Cal (3%), Qz (<1%), groundmass (23%)	Chl (7%), Wm*	Porphyritic; oscillatory zoning + sieve/embayed Pl; Cal + Opq clusters. Amp pseudomorph altered by Chl.
VP17-27	Gabbro	Pl (55%), Cpx (32%), Opq (<1%)	Chl (10%), Act (3%), Wm	Phaneritic; sericitized and sieve/embayed Pl; Cpx exsolution lamellae with Act rims and Chl alteration; fractures with Wm.
VP17-29	Basalt	Pl (50%), Cpx (14%), Cal (15%), Opq (6%), Bt (1%)	Chl (10%), Act (3%), Ep (1%), Wm.	Aphanitic and intergranular; sericitized; sieve Pl; resorbed Cpx; Cal-Chl-Act reaction clusters
VP17-30	Gabbro	Pl (50%), Cpx (23%), hbl (6), opq (6%), bt (1%)	Chl (9%), Act (3%), Ep (2%), Wm	Intergranular; Pl sericitized; Cpx embayed with act rim and Chl alteration; Cpx has Hbl coronas.
VP17-34	Basalt	Pl (49%), Cpx (29%), Opq (5%), Bt (2%)	Chl (10%), Act (4%), Ep (1%), Wm	Aphanitic; euhedral Pl with sieve cores; embayed Cpx with thin Act rim and Chl alteration
VP17-38	Gabbro	Pl (55%), Cpx (18%), Opq (8%), Hbl (2%), Bt (1%)	Chl (14%), Act (1%), Ep (1%), Wm	Equigranular; Pl sericitized; Cpx embayed with Act rim and altered by Chl
VP17-44	Gabbro	Pl (53%), Cpx (20%), Opq (10%), Bt (3%), Cal (1%)	Chl (9%), Act (2%), Ep (2%), Wm	Phaneritic; Extensive Pl sericitization; resorbed Cpx with Act rim and Chl alteration, two types of opq
VP17-45	Cryptocrystalline mafic lava	Vitric groundmass with Pl micro-phenocrysts, Cpx, Ox (no modal%)	Chl, Wm	Cryptocrystalline; flow banding, glass shards, welding textures, vitric matrix.
VP17-56	Gabbro	Pl (54%), Cpx (20%), Opq (9%), bt (1%)	Chl (13%), Act (3%), Ep (2%), Wm.	Intergranular; sericitized and sieve Pl; resorbed Cpx with Chl and Act alteration rims.
VP17-66	Welded lithic-crystal tuff	Angular Pl, Qz, volcanic lit, minor opq (no modal%)	Devitrified glass, Chl, and Wm	Fragmental, poorly sorted, devitrificated matrix

*Secondary fine-grained white mica (which constitutes sericitization) will not be included in the modal abundance % due to its fine-grained nature, as it is difficult to estimate its occurrence in the total % of the sample.

5.1.3 Representative micro photos



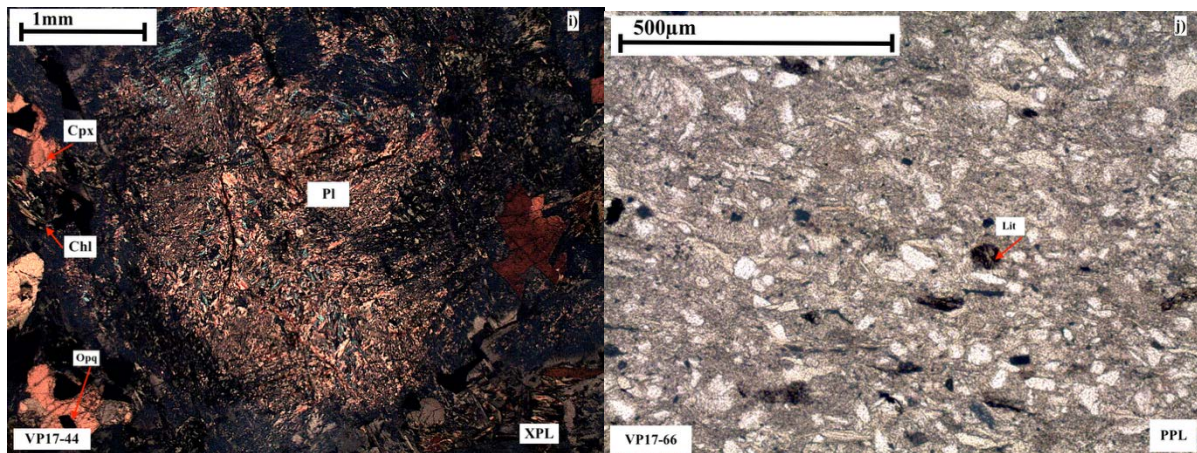


Figure 8: Representative images of the thin section a) porphyritic texture characterized by one elongated calcite phenocryst and several partly resorbed plagioclases with polysynthetic twins and sericitization set in a finer groundmass, b) extensive secondary alteration of clinopyroxene by fibrous chlorite, as well as actinolite reaction rims around the edges of clinopyroxene, c) cluster of clinopyroxene and calcite being replaced by secondary chlorite and actinolite, a plagioclase in the corner of the figure exhibits extensive sericitization at the center of the grain, d) simple twinning in clinopyroxene, with a hornblende corona and actinolite alteration along its fractures, e) plagioclase with sieve-texture, and chloritization and actinolite alteration of clinopyroxene, f) large clinopyroxene exhibiting embayment in which fibrous chlorite alters the grains. Other clinopyroxenes exhibit a thin reaction rim of actinolite, plagioclase shows extensive chloritization, and sericitization, g) angular quartz grains set in cryptocrystalline groundmass, flow banding can be observed, and chlorite alteration of the groundmass h) plagioclase exhibiting limited sericitization at the center of the grain, and chloritization along its edges, i) highly sericitized plagioclase now present as a pseudomorph of the primary mineral replaced by fine-grained white mica. Adjacent clinopyroxene exhibits chlorite alteration along embayed edges, j) tuffaceous texture with poorly sorted components of lithic fragments, and angular mineral grains set in a welded matrix.

5.2 Zircon textures and geochronology

The following section presents the CL images of the Svartevaeg sample (VP17-26b) and the tuffaceous sample from the Bourne Complex (VP17-66), along with their corresponding U-Pb SIMS data. To ensure the reliability of the U-Pb age data, it is displayed in Tera-Wasserburg Concordia diagrams and filtered according to several quality control criteria. Analyses were excluded if they exhibited significant discordance (greater than $\pm 10\%$), high uranium concentration (>1000 ppm), high common lead content ($> 5\%$), or large analytical uncertainties.

5.2.1 Svartevaeg Formation geochronology

Sample VP17-26b has an abundance of zircon grains in a variety of sizes. Most grains exhibit euhedral to subrounded external morphologies, accompanied by undisturbed growth zoning (oscillatory) with euhedral core-to-rim relationships. A few grains show evidence of fracturing or fluid interaction with inclusions and reaction rims and some grains have inherited cores surrounded by new growth rims. Figure 9 shows an average representation of the zircon grains in the sample.

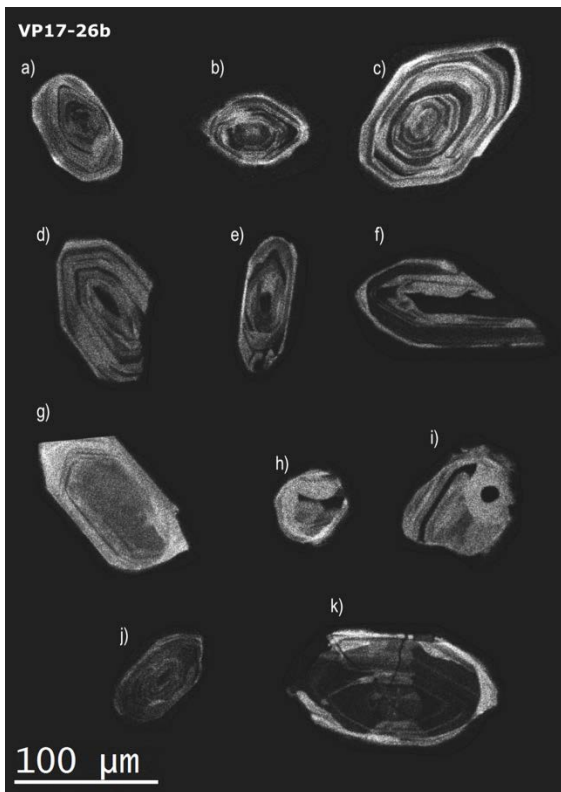


Figure 9: Representative image of the zircon textures in the VP17-26b. a-d) zircons with distinct oscillatory zoning with euhedral crystal morphologies e) faintly zoned core with limited resorption where a brighter CL rim truncate the core, f) a broken zircon grain, showing half a diagonal of a euhedral zircon with broad bands of oscillatory zoning, g) homogeneous core surrounded by fine oscillatory zoning, followed by a homogeneous brighter rim, h) sub-rounded fragmental grain with a cauliflower-like outer structure, i) zircon with a complex texture and distorted external morphology, it exhibit a dark core indicative of high uranium content, surrounded by homogenous growth that is truncated by faint oscillatory zoning, j) faint oscillatory zoning in an anomaly dark grain indicative of high uranium content, the grain was not suited for SIMS dating, k) fractured grain, with a partially resorbed outer rim and with a dark CL core with faint oscillatory zoning, the grains was not suited for SIMS dating.

For the SIMS, 21 U-Pb analyses were performed, and 19 of these indicated good reliability based on the quality control criteria (Figure 10a). The U-Pb analysis defines a tight cluster near the Concordia curve, with all analyses overlapping it within the analytical uncertainties. The sample yields a Concordia age of 431.3 ± 1.6 Ma (2σ confidence interval) with an MSWD of 1.04 and a P-value of 0.4. The dataset is relatively consistent, and there are no statistical reasons to reject the Concordia age. The observed scatter is within the expected range of analytical uncertainty, and there is no significant evidence of different age populations within the data. A kernel density diagram was plotted for the sample (Figure 10b). It exhibits a unimodal age distribution, with nearly all $^{206}\text{Pb}/^{238}\text{U}$ spot ages falling between 425 Ma and 437 Ma, and a pronounced peak at 431-432 Ma. The smoothed probability curve is symmetrical, closely overlaps the modal histogram bin, and mirrors the Concordia age of 431.3 ± 1.6 Ma obtained from the Tera-Wasserburg diagram. No subsidiary peaks or tails are present toward older or younger ages.

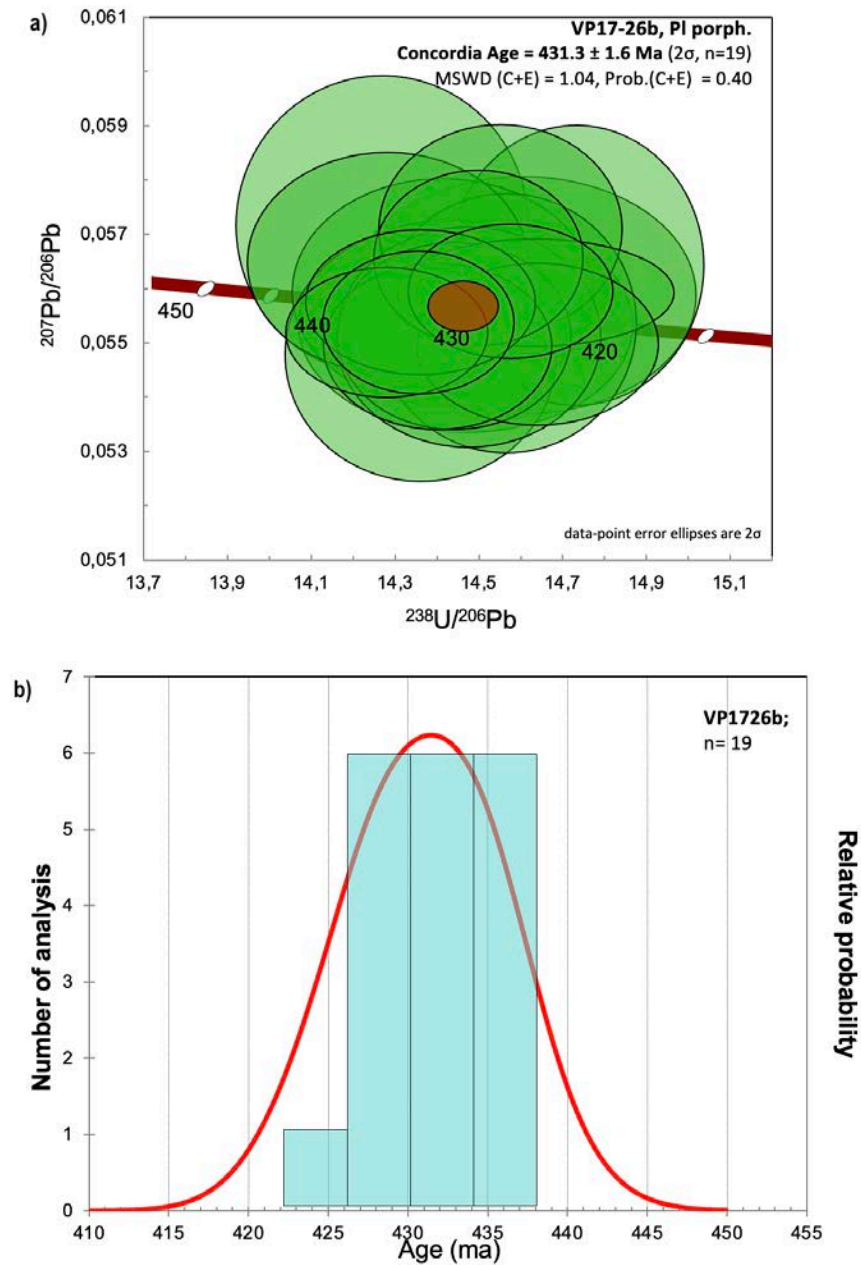


Figure 10: a) Tera-Wasserburg Concordia diagram of the filtered data from sample VP17-26b showing a tight cluster of analyses at the Concordia line and a Concordia age of 431.3 ± 1.6 Ma, b) kernel density diagram of the $^{206}\text{Pb}/^{238}\text{U}$ ages for sample VP17-26b, with the histogram of individual spot ages in blue and the smoothed probability density in red, showing a pronounced age peak at 431–432 Ma.

5.2.2 Bourne Complex geochronology

CL imaging was conducted on six samples from the Bourne (VP17-30, -38, -40, -56, and -66). Five of those samples had sparse zircon grains that were small (a diameter of around 10 μm) and were thereby unsuitable for subsequent U-Pb SIMS analysis. The VP17-66, however, yields abundant zircon grains that will be further described in this section.

The CL images of VP17-66 reveal a diverse population of mixed zircon textures, indicative of a detrital assemblage. A total of 56 zircon U-Pb analyses are obtained from the sample, and 21/56 analyses meet the quality control criteria (section 5.2). The unfiltered dataset (Figure 11) shows a wide spread of data points with evident discordance and large analytical uncertainties, indicating open-system behavior and a mixed-age population. The third parameter of the uranium content of each grain reveals that the most discordant ellipses correspond to U-rich grains (3-5.5 wt % U), whereas low-U zircons cluster closer to Concordia on the $^{238}\text{U}/^{206}\text{Pb}$ axis.

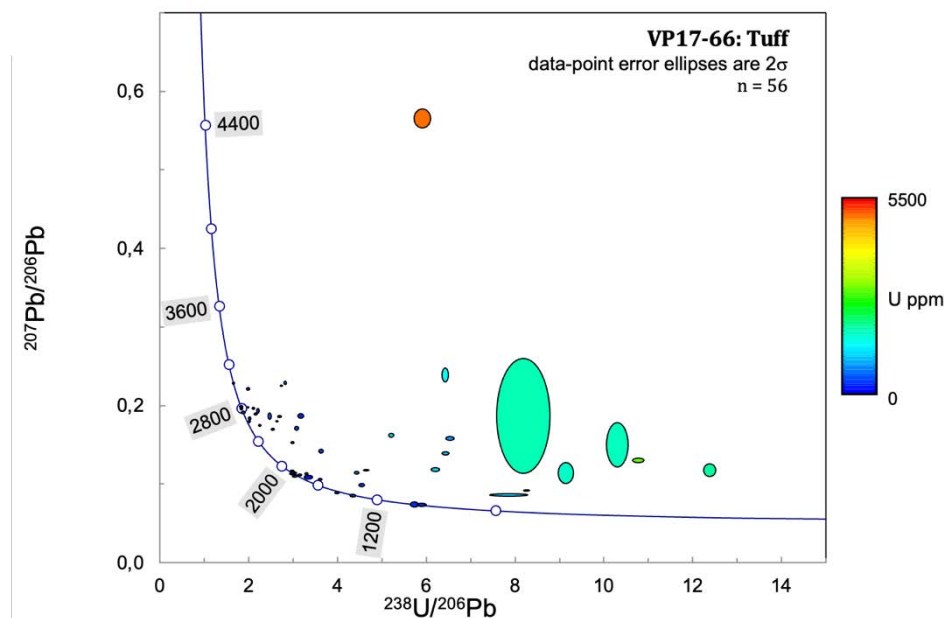
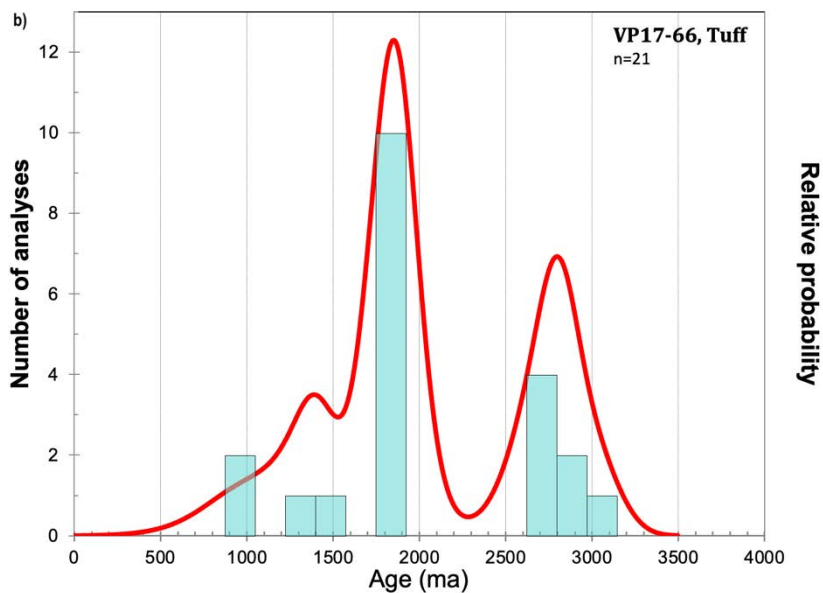
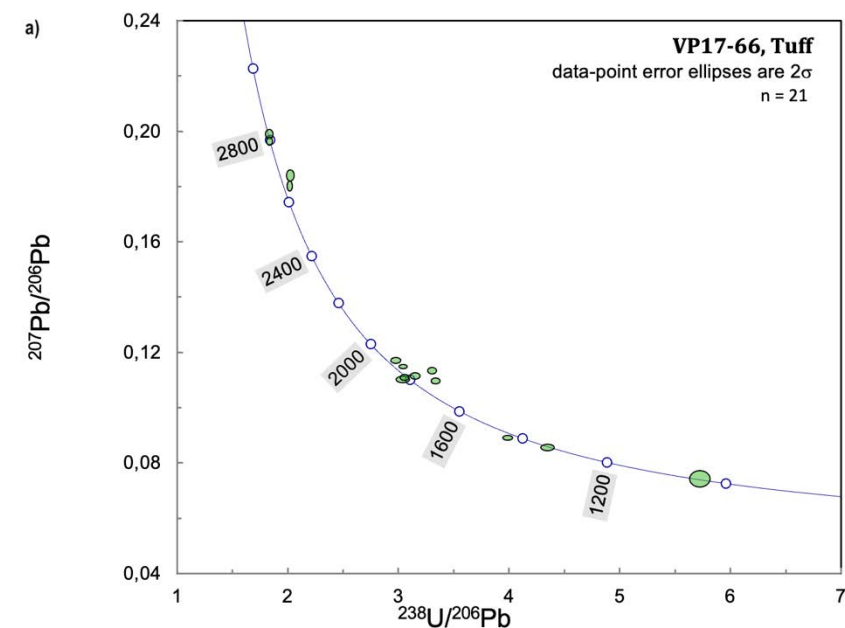


Figure 11: Tera-Wasserburg Concordia diagram of the unfiltered data from sample VP17-66, showing highly discordant data with large analytical uncertainties. The unfiltered data includes a third parameter of the uranium content, which shows increased discordance with higher uranium contents,

The filtered dataset of VP17-66 (Figure 12a) defines a tighter fit along the Concordia curve, indicating more reliable U-Pb data with an acceptable degree of concordance, lower uranium and common lead content, and lower analytical uncertainties. Due to the evidence for a mixed-age population, no Concordia age can be calculated. The youngest concordant grain in this sample is 1010.0 ± 12.4 Ma (2σ), but a single analysis is insufficient to define a MAD. A MAD estimate that incorporates both these 21 new analyses and previously U-Pb data on the same sample will instead be presented in Section 6.2.

The kernel density diagram (Figure 12b) shows two dominant age populations: a Neoproterozoic (2630-2770 Ma) (6 grains) and a Paleoproterozoic (1760-1930 Ma) (10 grains) age peak, with no Neoproterozoic or Paleozoic zircons present, aside from the lone 1010 ± 12.4 Ma grain. This indicates that the sample is dominated by recycled Paleoproterozoic and Neoproterozoic

detritus. The zircon texture obtained from the CL imaging is analyzed in relation to these age peaks (Figure 12c). The Neoproterozoic peak (c. 2770-2630 Ma) displays sharp, rhythmically bright oscillatory and sector zoning with a commonly euhedral external morphology; the banding is continuous and undisturbed across the grain. The Paleoproterozoic peak (c. 1930-1760 Ma) exhibits grains that show rounded or ovoid external morphologies, dark-luminescence, faintly zoned cores with partly resorption and overgrowth by irregular, brighter mantles. One core-rim crystal exhibits concentric “bull’s-eye” zoning with diffuse inner rings. The single Mesoproterozoic grain (1010 Ma) is small in size and exhibits homogeneous, high-luminescence textures, lacking any core-rim distinction or internal zonation.



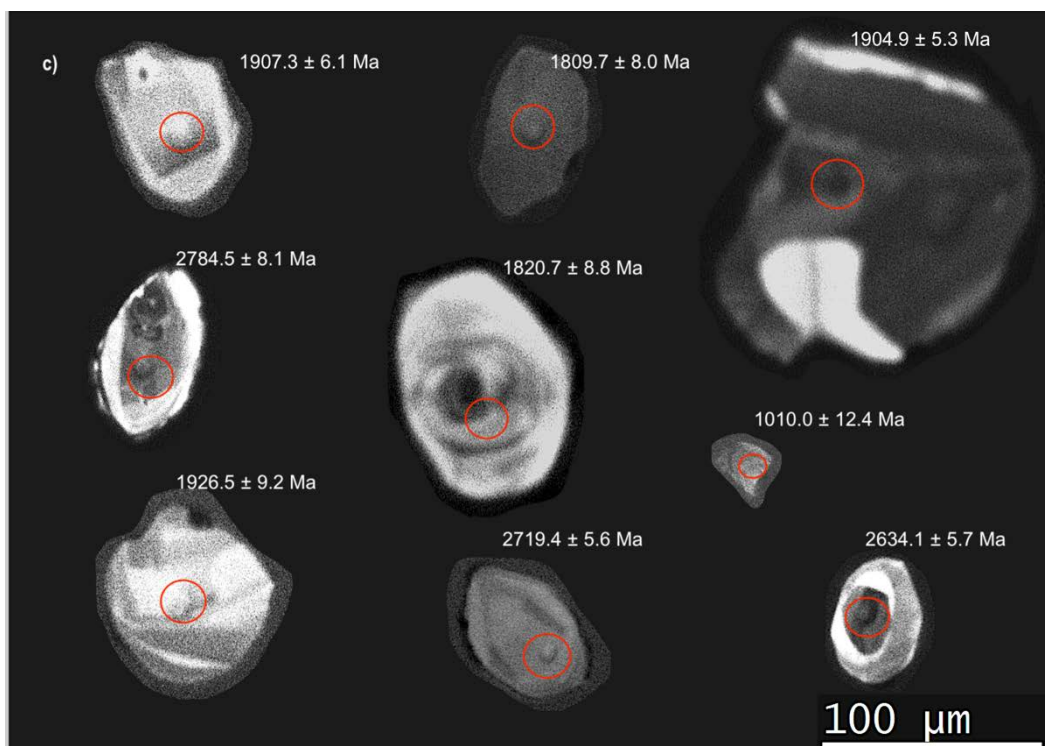


Figure 12: a) Tera-Wasserburg Concordia diagram of the filtered data from the VP17-66 sample (tuff). The analysis aligns or is placed near the Concordia line but with an evident detrital and mixed-age population and widespread age along the Concordia line, b) kernel density estimate diagram showing $^{207}\text{Pb}/^{206}\text{Pb}$ analysis spots density (blue histogram) and the relative probability curve (red), showing two age peaks at c.1760-1930 Ma and c.2630-2770 Ma, c) Representative CL images of the zircon grains from the age population peaks shown in Figure 12a-b, the analytical spot for the SIMS analysis is marked by the red circles.

6. Discussion

6.1 Textural evidence for disequilibrium and open-system behavior

The textural evidence is interpreted following Streak's (2008) description of disequilibrium and open-system indications in mineral textures, as well as Corfu et al.'s (2003) description of zircon textures.

6.1.1 Mineral textures in Svartevaeg Formation

This study is based on only one thin section from the Svartevaeg Formation (VP17-26b). Still, its petrography aligns with earlier descriptions provided by Trettin (1998), Hadlari and Madronich (2017), and Dewing et al. (2019). The sample is a plagioclase-porphyritic rock with plagioclase, pseudomorphs of amphibole and minor calcite and oxides within a fine-grained groundmass. A secondary alteration phase has entirely replaced the amphiboles by chlorite, and the plagioclases are altered by secondary fine-grained white mica. The phenocryst phase is interpreted to have grown slowly in a relatively stable reservoir

resembling a closed system, as indicated by growth zoning and, in some cases, fine oscillatory zoning in many plagioclase cores. The groundmass containing microlites reflects rapid ascent and quenching. The groundmass may reflect a subsequent injection of a hotter or more mafic composition, which could have driven the dissolution of the phenocrystic phase, creating the embayed, partially resorbed, and sieve-textured interiors observed in many of the plagioclase crystals, all indicating open-system behavior rather than entirely closed-crystal fractionation (Streck, 2008). Calcite phenocrysts riddled with oxide inclusions likely crystallized from a late, CO₂-rich fluid released during degassing of the magma, a feature Streck (2008) notes in many open-system lava suites.

The CL imaging reveals that most zircons in VP17-26b are igneous, characterized by euhedral external morphologies and distinct oscillatory zoning, typical of magmatic systems where the grains have grown in an undisturbed, relatively closed system (Corfu et al., 2003). A few grains exhibit thin bright outer rims that truncate darker, growth-zoned cores, indicating limited resorption followed by limited renewed zircon precipitation. There are rare xenocryst relics, as well as some patchy, late-stage recrystallized domains with subrounded exteriors, indicating fluid activity and metamorphic overprint.

Overall, sample VP17-26b documents a primary crystallization phase with initial oscillatory growth zoning in a closed magmatic system, followed by disruption and open-system resorption and possibly the degassing of CO₂. This has not affected the existing zircon crystals in the sample, confirming that the obtained zircon U-Pb ages from the sample correspond to an igneous crystallization event, with a reliable record of concordance (Schoene, 2014).

6.1.1 Mineral textures in Bourne Complex

The Bourne suite comprises five gabbroic plutonic rocks (VP17-27, -30, -38, -44, -56), three volcanic equivalents (VP17-29, -34, -45), and one welded lithic-crystal tuff (VP17-66). All samples exhibit a general primary phase consisting of plagioclase, clinopyroxene, and opaque oxides, with variable occurrences of calcite, hornblende, and biotite. All the samples exhibit several pieces of evidence for an open-system magmatic evolution, according to Streck's (2008) interpretations of disequilibrium textures. This includes spongy and sieve-textured plagioclase with corroded crystal faces and resorbed clinopyroxene with hornblende coronas, all of which are indicative of different open-system behaviors, such as magma

mixing, recharge of a hotter more mafic melt, or fluid infiltration. CL imagery of VP17-66 further reveals complex overgrowths and dissolution textures, and its highly discordant U-Pb data reinforce the interpretation of an open system.

A secondary alteration phase is evident across all samples, indicating significant post-crystallization alteration, particularly along fractures, which imposes greenschist-facies alteration with a hydrous phase overprint. This is marked by sericitization of plagioclase, extensive chloritization of clinopyroxene and plagioclase, chlorite-actinolite rims around clinopyroxene and fibrous secondary epidote associated with the sericitized areas. The alteration implies an active fluid phase, which in turn can mobilize lead (Schoene, 2014). The discordant U-Pb data in VP17-66 can partly be explained by fluid-assisted Pb loss, as these alteration fronts mark fluid pathways that can strip radiogenic lead from adjacent zircon domains (Schoene, 2014). The CL images of VP17-66 show embayed zircon grains with low-luminescent cores overgrown by bright, highly luminescent rims, indicating radiation damage and enhanced recrystallization (Corfu et al., 2003). This is further supported by the uranium content plot (Figure 11) linked to VP17-66, which correlates high discordance with extremely high uranium contents (3-5 wt% %). This correlation suggests that the U-rich grains, affected by radiation damage, experienced enhanced Pb mobility along diffusion pathways that promote fluid-mobilized Pb loss (Schoene, 2014; Stacey & Kramers, 1975).

6.2 Data reliability and age estimates

6.2.1 MAD evaluation

The reliability of a MAD estimate is significantly influenced by the number of zircon U-Pb analyses (n) used in the calculation. Larger sample sizes increase the statistical robustness of the derived age and reduce the likelihood of bias from outlier grains or analytical errors. Dodson et al. (1988) demonstrated that an MAD based on $n = 60$ provides a reasonably constrained estimate for age populations; however, for detrital samples, it still carries limitations regarding statistical certainty and the potential influence of lead loss or inheritance. Vermeesch (2004) expanded on this by evaluating that at least 117 grains are necessary to achieve robust statistical confidence in detrital zircon populations, especially in distinguishing true depositional populations from anomalously young grains potentially affected by lead loss. He addressed this by applying binomial probability theory to show how confidence in detecting zircon age populations scales with n . For example, to detect a

population that comprises 5% of the zircons with 95% confidence, at least 59 grains must be analyzed. To detect even rarer populations, which compose 1% at the same confidence level, approximately 299 grains are needed. Although this approach does not provide a confidence interval on the MAD itself, it underscores that a small n significantly limits the probability of sampling rare, potentially critical young grains. Pullen et al. (2014) further highlighted that datasets with approximately 1000 analyses are ideal for accurately resolving multiple age populations and capturing rare young grains, which are particularly important when estimating the MAD in recycled or poly-sourced sedimentary rocks. In short, confidence in the youngest age analyses improves significantly with larger n , whereas smaller datasets may yield misleadingly young ages due to random sampling of outliers.

In addition to sample size, the method used to determine the MAD also plays a critical role in the reliability of the result. Common approaches include selecting the youngest single grain, which provides the strictest possible constraint on sediment deposition; however, this method is the most susceptible to analytical error or Pb loss (Vermeesch, 2004). An alternative method is the weighted mean of the youngest cluster of analyses, which identifies the youngest group of concordant grains, generally based on a minimum of three analyses (Spencer et al., 2016), within overlapping uncertainty bounds (typically 2σ), thus increasing reliability by reducing reliance on a single analysis (Dodson et al., 1988). More recent work has proposed probabilistic methods, such as the youngest peak age from kernel density estimation or TuffZirc models, which aim to isolate the youngest true population from mixed-age datasets statistically (Pullen et al., 2014). These later approaches are especially advantageous in large- n datasets, where age spectra can be resolved into multiple overlapping age populations. Each method offers trade-offs between conservatism, reproducibility, and analytical uncertainty (Vermeesch, 2004; Pullen et al., 2014).

Notably, Vermeesch (2021) demonstrates that these earlier estimators for the MAD rely on order statistics drawn from the tail of the age data distribution. These methods are sensitive to the presence of outliers and become increasingly biased as sample size grows. Specifically, Vermeesch (2021) demonstrates that such estimators exhibit a systematic drift toward unrealistically young ages in large- n datasets, regardless of whether the data contain analytical artefacts or geological complexity. This is problematic for the weighted mean method, which assumes that the selected grains represent a coherent and geologically meaningful population. Without a formal probabilistic framework, it is not possible to assess

whether these grains reflect a true depositional signal or if they are affected by Pb loss, inheritance, or low-probability sampling. He mentioned an alternative method, the Maximum-Likelihood Age (MLA) method, that remains statistically unbiased regardless of sample size and improves in precision as n increases. In practice, Vermeesch suggests acquiring at least 80 high-quality zircon analyses that are filtered for $\pm <10\%$ discordance and <1000 ppm U or continuing until the propagated 2σ uncertainty on the MLA drops below 1% of the estimated age. Thus, while increasing n benefits probabilistic methods such as the MLA, it does not necessarily enhance the accuracy of previous estimators such as the weighted mean.

For this study, the results in Section 5.2.2 show a total of 21 concordant U-Pb zircon analyses obtained from the sample VP17-66. While this study may not capture the full spectrum of age population from sample VP17-66, are these analyses intended to be combined with a previous dataset by Victoria Pease on the same sample ($n = 69$), which passed the same quality-control filters (Section 5.2), yielding a total of $n = 90$ grains for this sample. The remaining grains were evaluated using both the youngest single grain and the youngest cluster approaches. The Tera-Wasserburg Concordia diagram of Pease's filtered dataset ($n = 69$) is shown in Figure 13a. The kernel density diagram of the same filtered dataset (Figure 13b) shows a mixed age population that resemble this study result with two evident age peaks at 1902-1818 Ma (18 grains) and one at 2776-2725 Ma (28 grains), with an additional younger population at 580-600 Ma (4 grains). There are minor Mesoproterozoic peaks (1100-1300 Ma) present, but each comprises less than three ages and does not form a distinct age population (Spencer et al., 2016).

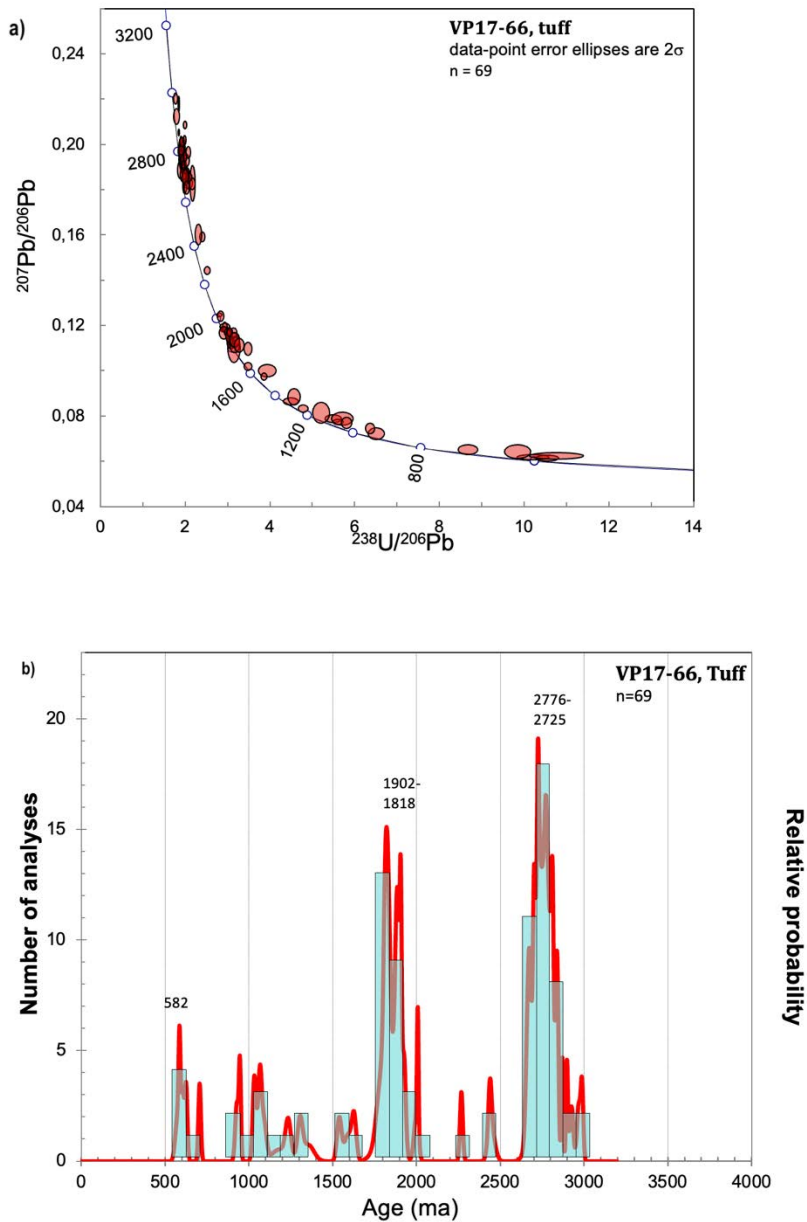


Figure 13: a) Tera-Wasserburg Concordia diagram of the filtered dataset from V.P. (personal communication, 2025-04-30), of the VP17-66 sample, b) kernel density diagram from V.P. (personal communication, 2025-04-30) of the filtered dataset of VP17-66 sample showing three distinct population age peaks, with the youngest peak at 560-580 Ma (based on four grains).

The youngest analyses from the kernel density diagram that meet the statistical requirement of three concordant grains (spencer et al., 2016) comprise ages of 573.8 ± 13.3 Ma, 585.7 ± 5.8 Ma, and 604.4 ± 8.7 Ma. A weighted mean calculated from these yields an MAD of 589.4 ± 9.2 Ma (2σ), with an MSWD of 2.4 and a p-value of 0.09, indicating excess scatter and weak statistical equivalence. If the calculation is limited to the two youngest spots (573.1 ± 13.3 Ma and 585.8 ± 5.9 Ma), the resulting MAD yields an age of 584 ± 11 Ma (MSWD = 0.74; p = 0.39), which is a stronger statistical value more indicative of a single age population. However, the two youngest analyses come from two SIMS spots on a single

zircon grain (core and rim) (Figure 14). The grain that defines the MAD exhibits medium-luminescence and oscillatory zoning from core to rim, indicative of a relatively undisturbed igneous system (Corfu et al., 2003). Two SIMS spots were placed on adjacent growth bands: the outermost rim (573.1 ± 13.3 Ma) and an interior band of the core (585.8 ± 5.9 Ma). Because the two ages overlap within analytical uncertainty and no metamorphic overgrowths, patchy recrystallization, or veinlets are present, the entire grain is interpreted as a single detrital igneous zircon that crystallized during a late-Ediacaran magmatic event and was later incorporated in the tuffaceous sample.

Despite the increase from 21 to 90 concordant analyses for the VP17-66 sample, the reliance on a single grain to define the MAD is problematic. As discussed by Dodson et al. (1988) and Vermeesch (2004), the youngest single grain may reflect analytical artefacts, lead loss, or inheritance, and does not provide a robust constraint unless supported by multiple grains of similar age. Even with the combined dataset of $n = 90$, the number of concordant grains also remains marginal, and the confidence level in the resulting MAD remains statistically limited, as there may be additional age populations present in the sample that were not represented in the sampling. As shown by Vermeesch (2004), datasets with fewer than 117 grains are vulnerable to under-sampling the youngest age population and may not reliably constrain the true depositional age (TDA), particularly in multi-sourced or recycled sedimentary systems. Thus, while the combined dataset ($n = 90$) represents an improvement in analytical coverage, the resulting MAD should be interpreted with caution and viewed as an approximate and tentative maximum age, pending additional analyses that could verify the presence of a more substantial population of Ediacaran zircons. It may benefit from reevaluation using likelihood-based methods (Vermeesch, 2021) if additional data become available.

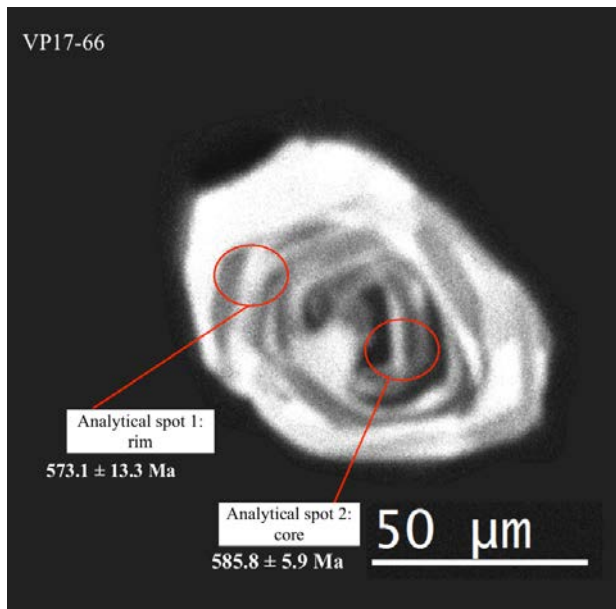


Figure 14: CL image showing the analytical spot from the SIMS for the two youngest analyses of VP17-66 from the V.P. dataset. The two analyses are from the same grain, showing a core and rim relationship.

6.2.2 Older age populations and provinces

The grains assigned to the Neoproterozoic (c. 2630-2770 Ma) age peak are euhedral to subrounded and dominated by bright oscillatory zoning that encircles darker, weakly zoned interiors. The zoning is continuous and lacks cross-cutting veinlets or resorption surfaces, matching Corfu et al. (2003) description of unmodified magmatic crystals grown in a stable closed system from a zirconium-saturated melt. In contrast, the grains assigned to the Paleoproterozoic (c.1750-1930 Ma) peak exhibit much more complex CL patterns: some possess concentric oscillatory zoning, whereas others contain low-luminescence cores with abrupt truncation by bright, high-luminescence overgrowths. Several grains exhibit embayed margins and narrow metamorphic rims. These features correspond to Corfu et al. (2003) description of a corroded xenocryst core with recrystallized or metamorphically overgrown zircon growth, indicating partial recrystallization or fluid-enhanced overgrowth following the original igneous crystallization event. Together, these textures confirm that the Neoproterozoic zircons record a relatively unmodified igneous system, while the Paleoproterozoic population indicates later recrystallization or hydrothermal modification.

6.2.3 Timing of U-Pb disturbance

As Pb loss has been corrected for (Stacey & Kremer, 1975), can the discordance be used to give information on potential thermal disruption or metamorphic alteration events (Schoene, 2014). To investigate the discordant data, the unfiltered data from Pease's combined dataset

are plotted (Figure 15a). The discordance is widespread, but a Discordia line can be constructed based on seven grains. These grains were selected because they define a coherent linear trend in the Tera-Wasserburg diagram, suggesting they may share a common Pb-loss history. As discussed by Schoene (2014), the formation of a meaningful Discordia requires selecting analyses that lie along a linear array, ideally representing isotopic compositions affected by a single disturbance event. The grains used for the Discordia line span a wide discordance range but align well with a lower intercept at 550 ± 36 Ma (MSWD = 1.14, $p = 0.34$), suggesting that they could have recorded a shared thermal or fluid-related resetting event. However, there is a large margin of error, and the age is not well-defined.

In Figure 15b, a third parameter of the uranium content is applied to the unfiltered dataset. It shows that several of the discordant grains that make up the Discordia line have high U contents (>1000 ppm). High-U grains are prone to radiation damage, which enhances Pb mobility and generates discordance without the occurrence of large-scale metamorphism (Schoene, 2014). Based on the statistical parameters (MSWD and the p-value), there is no strong indication to reject the Discordia age, and the lower intercept of 550 ± 36 Ma could reflect the time of a fluid/thermal disturbance (Schoene, 2014). However, as emphasized by Vermeesch (2020), applying Discordia regression to detrital zircon data requires caution, since detrital grains are typically not cogenetic and may have experienced different geological histories. The assumption that these grains record a single disturbance event is therefore speculative, particularly in the absence of supporting petrographic or stratigraphic evidence. This result may reflect a post-depositional Pb-loss signal, potentially enhanced by high-U contents and radiation damage, rather than a uniform metamorphic or thermal event.

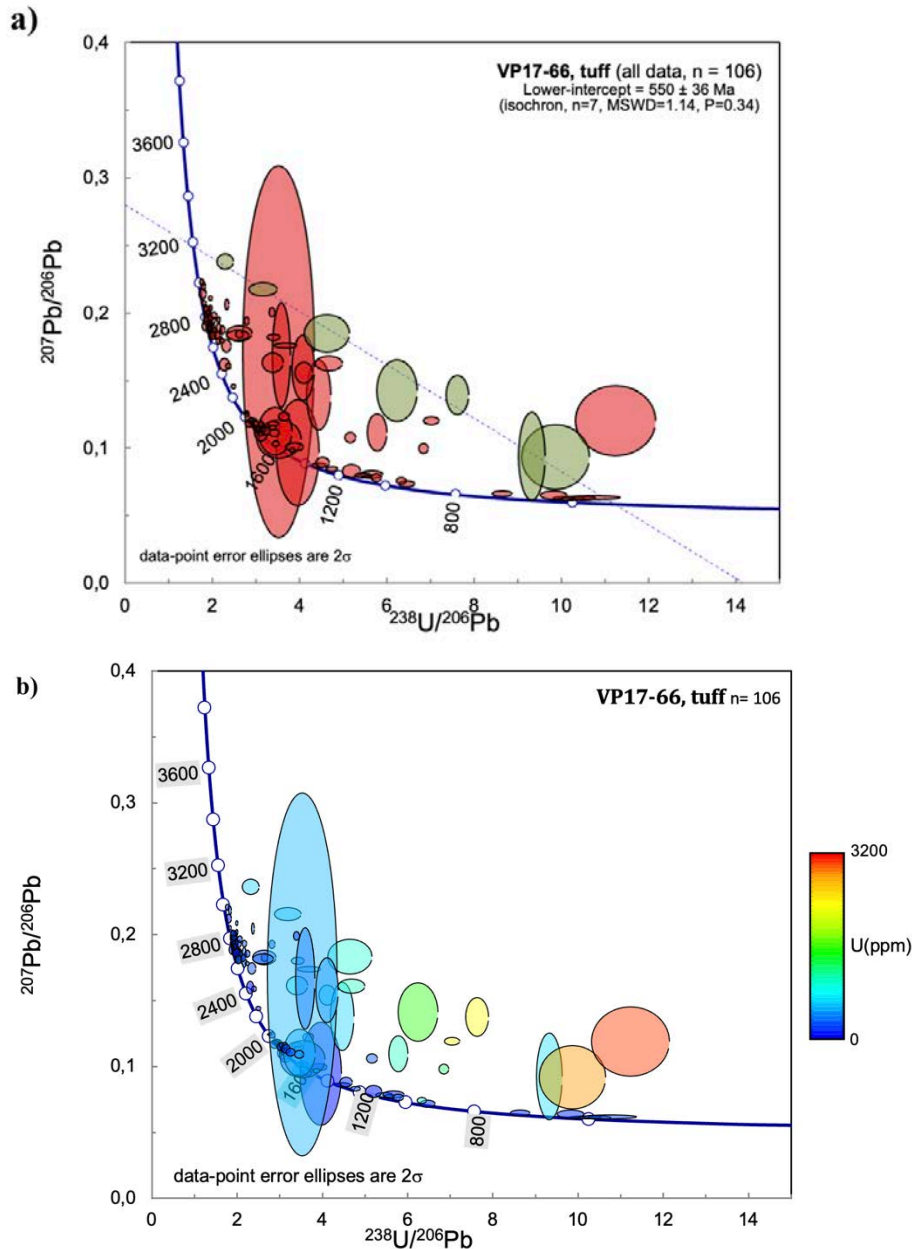


Figure 15: a) Tera-Wasserburg Concordia diagram of the unfiltered dataset ($n=106$) from Victoria Pease (personal communication 2025-04-30) showing a constructed Discordia line through seven analyses (green ellipses) with a lower intercept at 550 ± 36 Ma, b) the uranium content of the unfiltered data of VP17-66 showing high uranium content (>1000 ppm U) in many of the seven grains that the Discordia line (Figure 15a) is based on.

6.3 Regional tectonomagmatic constraints

The Neoproterozoic and Paleoproterozoic age peaks, as well as the tentative Ediacaran MAD of 584 ± 11 Ma, are all older than most of the Pearya terrane and the Franklinian basin, which are primarily Cambrian to Ordovician in age (Koch et al., 2024). However, the Pearya terrane, particularly Succession II, contains metasedimentary units with significant detrital zircon populations between 550 and 650 Ma (Koch et al., 2024; Estrada et al., 2018). This corresponds with the tentative MAD, suggesting that the Bourne Complex may be correlative

the early successions of the Pearya terrane. However, the MAD also aligns with the earliest phase of rifting and continental fragmentation along the Franklinian margin, as recorded in the Yelverton Formation (Faehnrich et al., 2023). Yelverton Formation is interpreted to have formed during the late Ediacaran to early Cambrian rifting (c. 574-530 Ma) and is comprised of mafic flows and volcanics interbedded with carbonated and siliciclastic rocks (Faehnrich et al., 2023). The structural proximity where the Bourne Complex sits immediately north of the main Yelverton exposures in the Franklinian Basin, both aligned along the same structural trend that localized early rift-related volcanism, further strengthens their potential relationship.

Although the MAD of 584 ± 11 Ma ($n = 2$ youngest analyses) must be viewed as tentative, it nonetheless predates the emplacement of the volcanic rocks of Mount Rawlinson, which recent research investigates for a possible connection to the Bourne. $^{40}\text{Ar}/^{39}\text{Ar}$ hornblende ages from Mount Rawlinson cluster at 454-450 Ma (Powell & Schneider 2022), recording a Late Ordovician-Silurian arc pulse that overprints the older Franklinian sequence. Thus, while the Bourne Complex captures a late Ediacaran depositional event, the Mount Rawlinson volcanics represent a distinct, much younger Ellesmerian-age magmatic episode that, at present, cannot be linked to the Bourne Complex.

The VP17-66 sample, however, is dominated by pronounced Neoproterozoic (c.2630-2770 Ma) and Paleoproterozoic (c.1750-1930 Ma) age populations. Such ancient ages cannot be sourced from the Pearya basement, which is predominantly Tonian to Neoproterozoic in age (Koch et al., 2022). Instead, Koch et al. (2024) demonstrate that fault-bounded units in the Petersen Bay, Kulutingwak Fiord, and Emma Fiord zones (all on northwestern Ellesmere Island) exhibit dominant modes at 1800-1900 Ma and 2700 Ma. These are attributed to the erosion of proximal Archean and Paleoproterozoic crustal blocks from the Canadian basement (Rae-Hearne orthogneisses) exposed along the Franklinian margin south of Ellesmere Island. Moreover, both Beranek et al. (2013) and Anfinson et al. (2012) document that Lower Cambrian deep-water units in the Franklinian Basin, specifically the Nesmith Beds and the Grant Land Formation, carry diagnostic detrital-zircon age distributions characterized by a Neoproterozoic peak at 2500-2800 Ma (centered at 2700 Ma; comprising roughly 20-40 % of all grains), and a Paleoproterozoic peak at 1600-2000 Ma (with a dominant mode at 1850-1920 Ma, often representing 25-60 % of grains). These modes are also interpreted as originating from the erosion of the Rae and Hearne orthogneisses, which

were exposed along the Franklinian margin during Early Cambrian subsidence (Anfinson et al., 2012; Beranek et al., 2013). Furthermore, the Bourne Complex outcrops lie in direct faulted contact with these same Franklinian-basin units (Powell & Schneider, 2022), which could strengthen that the detrital signal observed in VP17-66 of Neoproterozoic and Paleoproterozoic ages, records sediment transport along the same northerly Shield input corridor.

In the context of previous dating of the Bourne Complex, the tentative MAD of 584 ± 11 Ma is significantly older than the previously reported argon ages. Henry (1991) reported a $^{40}\text{Ar}/^{39}\text{Ar}$ age of 380 ± 10 Ma for phenocrystic hornblende in porphyritic andesite from the Bourne Complex. These data had notable dispersion and a suspected thermal overprint which Trettin (1998) argued showed argon loss caused by later dyke intrusion; the date therefore reflected partial resetting rather than crystallization or peak metamorphic ages. Powell and Schneider (2022) obtained a weighted-mean muscovite fusion age of 439 ± 2 Ma from a volcanoclastic unit adjacent to the Kleybolte Fault from the Bourne Complex. They interpreted this age as recording post-accretionary cooling, likely linked to late Ordovician-Silurian arc activity associated with Pearya-related faulting, rather than primary crystallization. Because the muscovite $^{40}\text{Ar}/^{39}\text{Ar}$ geochronometer can track several geological processes, including post-metamorphic cooling, dynamic recrystallization and deformation, thermal or fluid-driven argon diffusion, and detrital cooling histories (Powell & Schneider, 2022) a single-step (total-fusion) approach cannot distinguish between (1) true cooling through muscovite's closure temperature (300°C), (2) retention of older, relict argon domains, or (3) partial resetting during later thermal or fluid events (Kelley, 2002). If any grain contained a small amount of inherited or excess ^{40}Ar , its fusion age would appear anomalously old; likewise, partial argon loss would produce anomalously young ages. The tight clustering of the seven fusion ages at 439 ± 2 Ma can indicate either that a similar mid-Silurian thermal pulse wholly reset each grain, or that all grains carried a consistent, minor excess or relict argon component, or that this represents a completely closed system. However, without the step-heating spectra, minor excess argon or partial resetting cannot be ruled out (Kelley 2002).

Moreover, on northern Ellesmere Island, multiphase deformation and prolonged fluid flow along reactivated faults are known to disturb the argon system of muscovite (Estrada et al. 2018). Due to argon's sensitivity to reheating and argon loss, the $^{40}\text{Ar}/^{39}\text{Ar}$ system does not

provide reliable age constraints if there is no evidence of complete system closure (White, 2015). Powell and Schneider (2022) specifically emphasize that the Kleybolte Fault and adjacent units, where the Bourne Complex muscovite sample was collected, exhibit a prolonged and overprinting thermal history, further complicating their result.

The sample from the Svartevaeg Formation (VP17-26b) was investigated in this study because it is theoretically related to the Bourne Complex (Trettin, 1996). The CL imaging of the Svartevaeg sample provides evidence for undisturbed igneous zircon textures, thus the U-Pb age is a crystallization age. The U-Pb zircon Concordia diagram revealed a single cluster of analyses overlapping the Concordia curve, yielding an igneous crystallization age of 430.2 ± 1.6 Ma (MSWD = 0.47, P-value = 0.92); the statistics indicate good data quality with minimal scatter. This suggests that the zircons have remained in a closed system since formation, and that this records a primary igneous crystallization event, without significant Pb loss, metamorphic overprint, or alteration (Schoene, 2014).

Detrital zircons from Svartevaeg previously yielded an MAD of 428 ± 6 (Dewing et al., 2019), which is in excellent agreement with the obtained age of 430.2 ± 1.6 Ma. This age aligns with the regional Silurian magmatism associated with arc-related activity following the accretion of Pearya during the M'Clintock orogeny (Koch et al., 2024). A Silurian volcanic arc was active across the northern Laurentian margin post-Pearya accretion, resulting in the formation of different volcanic and volcanoclastic rocks. (Koch et al., 2022). The age of the Svartevaeg sample (VP17-26b) agrees specifically with the timing of Silurian arc-related magmatism associated with the Lands Lokk and Danish River Formations, both of which yield MADs of 425-441 Ma and are interpreted as Upper Llandovery-Ludlow flysch units derived from ongoing arc activity when back-arc extension, transgression, and strike-slip faulting followed the Pearya accretion (Faehnrich et al., 2023; Koch et al., 2022). This supports the idea that the phase of arc magmatism occurred regionally after the Pearya accretion, implying a shared magmatic system across Northern Laurentia and the Arctic Islands during mid-Silurian time (Koch et al., 2024; Powell & Schneider, 2022). This could be relevant to the tectonomagmatic evolution of the Bourne Complex, which may be associated with the same Silurian arc framework.

At present, however, there is no direct link between the Bourne Complex and the Svartevaeg Formation. The tuffaceous sample (VP17-66) from the Bourne Complex provides only a single-grain MAD of 584 ± 11 Ma. Nevertheless, the spatial proximity and the shared

structural trend of the Bourne Complex and the Svartevaeg Formation hint at a possible common arc framework, possibly following the accretion of Pearya. Resolving whether the Bourne Complex represents an outlying segment of the Silurian arc and is genetically linked to or merely juxtaposed against the Svartevaeg Formation, will require additional U-Pb dating of zircons from its volcanic and plutonic units.

7. Conclusions

The uncertain age of the Bourne Complex and its potential relationship to the Svartevaeg Formation were investigated employing U-Pb zircon geochronology. The following conclusions have been made:

- 1. Late Ediacaran MAD:** Detrital-zircon U-Pb analyses of a tuffaceous sample from the Bourne Complex yield a tentative MAD of 584 ± 11 Ma ($n = 2$ youngest analyses).
 - The late Ediacaran MAD aligns with both detrital metasedimentary units from the Pearya (Succession II) and an early phase of rifting along the Franklinian margin, as recorded in the Yelverton Formation.
 - A larger sample size is needed to confirm the MAD. A younger age population may be present that was not represented in this study, or alternatively, this MAD represents only an anomalous young grain affected by lead loss or analytical artefacts.
- 2. Detrital-Zircon Provenance:** Two dominant modes from the Bourne sample of 2630-2770 Ma and 1750-1930 Ma match Lower Cambrian Franklinian units (Nesmith Beds, Grant Land Formation), indicating inheritance from the Canadian Shield (Rae-Hearne basement).
- 3. Discordance:** The tuffaceous sample from the Bourne exhibits highly discordant and uranium-rich data, confirming open-system behaviors.
 - A Discordia line was constructed ($n=7$) with a lower intercept at 550 ± 36 Ma, interpreted as Pb loss from U-rich, radiation-damaged zircons, not a regional metamorphic pulse.

- 4. Relationship to the Svartevaeg Formation:** A plagioclase-porphyritic rock from the Svartevaeg Formation yields a concordant age of 431 ± 1.6 Ma, interpreted as the time of crystallization, and it is consistent with Silurian arc magmatism across the region. At present, a direct comparison with The Bourne Complex cannot be made within this context.

7.1 Implications and future work

If additional analyses confirm the tentative MAD for the Bourne Complex of 584 ± 11 Ma, the Bourne Complex demonstrably exhibits a possible late-Ediacaran deposition and is considerably older than the Cambrian-Ordovician arc suites of northern Ellesmere Island. Further analyses should focus on trace-element chemistry to interpret source terranes to possibly confirm a cogenetic relationship with the Pearya terrane (succession II) or the early phase of rifting along the Franklinian margin, both of which demonstrate a late Ediacaran age.

Moreover, if the obtained U-Pb age from the Svartevaeg Formation of 431 ± 1.6 Ma resembles a primary crystallization phase, it places it in a larger regional context of Silurian arc magmatism linked to the post-accretion of the Pearya Terrane. Further analyses of the Bourne Complex, which targets volcanic or plutonic samples, facilitate the investigation of a potential relationship with the Svartevaeg Formation and a possibly shared Silurian magmatic arc system.

Acknowledgments

I want to express my deepest gratitude to my supervisor Victoria Pease. She has contributed with broad knowledge, great patience, and has continuously deepened my understanding of both the geological context and the methodological matters. I would also like to thank Martin Whitehouse from the NORDSIMS Laboratory at NRM, who set up the SIMS procedure and provided all the data from that analytical session. I would also like to thank Kerstin Lindén from NRM, who prepared all the samples for the SEM and SIMS analysis and assisted with the analytical procedure for the SEM setup.

References

- Anfinson, O.A., Leier, A., Embry, A., Dewing, K. (2012). Detrital zircon geochronology and provenance of the Neoproterozoic to Late Devonian Franklinian Basin, Canadian Arctic Islands. *Geological Society of America Bulletin*, 124(3/4): pp. 415-430. DOI: 10.1130/B30503.1
- Beranek, L.P., Pease, V., Scott, R.A., Thomsen, T.B. (2013). Detrital zircon geochronology of Ediacaran to Cambrian deep-water strata of the Franklinian basin, northern Ellesmere Island, Nunavut: implications for regional stratigraphic correlations. *Canadian Journal of Earth Sciences*, 50(10): pp. 1007-1018. DOI: 10-1139/cjes-2013-0026
- Cawood, P.A., Hawkesworth, C.J., Dhuime, B. (2012). Detrital zircon record and tectonic setting. *Geology*, 40(10): pp. 875-878. DOI: 10.1130/G32945.1
- Corfu, F., Hanchar, J.M., Hoskin, P.W.O., Kinny, P. (2003). Atlas of zircon textures. *Mineralogy and Geochemistry*, 53(1): pp. 468-500. DOI: 10.2113/0530469
- Dewing, K., Hadlari, T., Pearson, D.G., Matthews, W. (2019). Early Ordovician to Early Devonian tectonic development of the northern margin of Laurentia, Canadian Arctic Islands. *Geological Society of America Bulletin*, 131(7-8): pp. 1075-1094. DOI: 10.1130/B35017.1
- Dodson, M.H., Compston, W., Williams, I.S., Wilson, J.F. (1998). A search for ancient detrital zircons in Zimbabwean sediments. *Journal of the Geological Society*, 145(6): pp. 977-983. DOI: 10-1144/gsjgs.145.6.0977
- Estrada, S., Piepjohn, K., Henjes-Kunst, F., & von Gosen, W. (2003). Geology, magmatism and structural evolution of the Yelverton Bay area, northern Ellesmere Island, Arctic Canada. *Polarforschung*, 73(2/3): pp. 59-75.
- Estrada, S., Mande, K., Gerdes, A., Gärtner, A., Hoffmann, M., Spiegel, C., Damaske, D., Koglin, k. (2018). Proterozoic to Cretaceous evolution of the western and central Pearya Terrane (Canadian High Arctic). *Journal of Geodynamics*. 120: pp. 45-76. DOI: 10.1016/j.jog.2018.05.010
- Faehnrich, K., McClelland, W.C., Webb, L., Kościńska, K., Strauss, J.V. (2023). Late Ediacaran-early Cambrian rifting along the northern margin of Laurentia: constraints from the Yelverton Formation of Ellesmere Island, Canada. *Canadian Journal of Earth Science*, 60 (12): pp. 1597-1626. DOI: 10.1139/cjes-2023-0020
- Hadlari, T., Madronich, L.I. (2017). Stratigraphic revision of the Franklinian stratigraphy of the northern Axel Heiberg fold belt, Nunavut. *Geological Survey of Canada, Open File 8238*, DOI: 10.4095/300534

Henry, A.S. (1991). *The Petrochemistry and Origin of the Bourne Complex, Northwestern Ellesmere Island, Canada*. [Bachelor's Thesis]. Halifax, Nova Scotia: Dalhousie University.

Ireland, T.R., Williams, I.S. (2003). Considerations in zircon geochronology by SIMS. *Mineralogy and Geochemistry*, 53 (1): pp. 215-241. DOI: 10.2113/0530215

Kannan, M. (2018). Scanning electron microscopy: Principle, components and applications. In Subramanian et al. (Eds.) *A textbook on fundamentals and applications of nanotechnology*: pp. 81-92. Springer.

Kelley, S. (2002). Excess argon in K-Ar and Ar-Ar geochronology. *Chemical Geology*, 188(1): pp. 1-22. DOI: 10.1016/S0009-2541(02)00064-5

Koch, M.M., McClelland, W.C., Gilotti, J.A., Kościńska, K., Strauss, J.V., Faehnrich, K., Beranek, L.P., Pease, V. (2024). Early Paleozoic accretionary history of the Pearya terrane: New insights from igneous and detrital zircon signatures of the Kulutingwak Formation, Ellesmere Island, Nunavut, Canada, *Geosphere*, 20 (3): pp. 778-798. DOI: 10.1130/GES02723.1

Koch, M.M., Faehnrich, K., McClelland, W.C., Crowley, J.L., Melchin, M.J., Beranek, L.P., Strauss, J.V. (2022). Age and significance of the Fire Bay assemblage: an Ordovician arc fragment within the Clements Markham belt, northwestern Ellesmere Island, Canada. *Canadian Journal of Earth Science*, 59: pp. 639-659. DOI: 10.1139/cjes-2021-0129

Ling, X.X., Ma, H.X., Liu, Y., Li, Q.L. (2020). Electrostatic force: A novel method for mounting small zircon grains to expose the maximum outer surface, *Solid Earth Sciences*, 5 (3): pp. 226-231. DOI: 10.1016/j.sesci.2020-08-005

Ludwig K R 2011 Isoplot/Ex Version 4.15: A Geochronological Toolkit for Microsoft Excel: Geochronology Center; Berkeley, California, USA.

Microscopy Australia. (n./d.). Secondary-ion mass-spectrometer schematic [Illustration]. In SIMS: Common features of the Large Geometry and NanoSIMS. *MyScope Training*. Retrieved 2025-05-29, retrieved at: https://myscope.training/SIMS_Common_features_of_the_Large_Geometry_and_NanoSIMS (2025-06-02).

Powell, J.W., Schneider, D.A. (2022). Phanerozoic Record of Northern Ellesmere Island, Canadian High Arctic, Resolved Through 40 Ar/ 39 Ar and (U-Th)/He Geochronology. *Tectonics*, 41(9). DOI: 10.1029/2021TC007065

Pullen, A., Ibáñez-Mejía, M., Gehrels, G.E., Ibáñez-Mejía, J.C., Pecha, M. (2014). What happens when n=1000? Creating large-n geochronological datasets with LA-ICP-MS for geologic investigations. *Royal Society of Chemistry*, 29: pp. 971-980. DOI: 10.1039/c4ja00024b

- Pupin, J.P. (2024). Zircon typology: a synthesis. Applications to magmatic, metamorphic and sedimentary rocks. *Journal of Petrology*, 65(11): pp. 1-22. DOI: 10.1093/petrology/egae111
- Schoene, B. (2014). U-Th-Pb geochronology. In Holland HD & Turekian KK (Eds.), *Treatise on geochemistry*, 4(2): pp. 341-378. DOI: 10.1016/B978-0-08-095975-7.00310-7
- Sharman, G.R., Malkowski, A.M. (2020). Needles in a haystack: Detrital zircon U-Pb ages and the maximum T depositional age of modern global sediment. *Earth-Science Reviews*, 203, 103109: pp. 1-23. DOI: 10.1016/j.earscirev.2020.103109
- Schiffer C, Stephenson R, Oakey GN, Jacobsen BH. 2016. The crustal structure of Ellesmere Island, Arctic Canada-teleseismic mapping across a remote intraplate orogenic belt. *Geophysical Journal International*, 204(3): pp. 1579-1600. DOI: 10.1093/gji/ggv539
- Schaltegger, U., Schmitt, A.K., Horstwood, M.S.A. (2015). U-Th-Pb zircon geochronology by ID-TIMS, SIMS, and laser ablation ICP-MS: Recipes, interpretations, and opportunities. *Chemical Geology*, 402: pp. 89-110. DOI: 10.1016/j.chemgeo.2015.02.028
- Smol, J.P., Douglas, M.S.V. (2007). Crossing the final ecological threshold in high Arctic ponds. [Map]. *Proceedings of the National Academy of Sciences*, 104(30): pp. 12395-12397. DOI: 10.1073/pnas.0702777104
- Spencer, C.J., Kirland, C.L., Roberts, N.M.W. (2016). Strategies towards statistically robust interpretation of in situ U-Pb zircon geochronology. *Geoscience Frontiers*, 7(4), pp. 581-589. DOI: 10.1016/j.gsf.2015.11.006
- Stacey, J.S., Kramers, J.D. (1975). Approximation of Terrestrial Lead Isotope Evolution by a Two-Stage Model. *Earth and Planetary Science Letters*, 26(2): pp. 207-221. DOI: 10.1016/0012-821x(75)90088-6
- Streck, M.J. (2008). Mineral textures and zoning as evidence for open-system processes. *Mineralogy & Geochemistry*, 69(1): pp. 595-622. DOI: 10.2138/rmg.2008.69.14
- Trettin, H.P., Gabites, J., Norford, B. (1998). Pre-Carboniferous Geology of the Northern Part of the Arctic Islands, Northern Heiberg Fold Belt, Clements Markham Fold Belt, and Pearya, Northern Axel Heiberg and Ellesmere Islands. *Geological Survey of Canada Bulletin*, 425: 401.
- Trettin, H. P. (1996). Geology, Cape Stallworthy - Bukken Fiord, District of Franklin, Northwest Territories. *Geological Survey of Canada, "A" Series Map*, 1884A, Natural Resources Canada. DOI: 10.4095/208958

Trettin, H.P. (1994). Major stratigraphic-structural provinces of Queen Elizabeth Islands and North Greenland [Map]. In Pre-Carboniferous geology of the northern part of the Arctic Islands: Hazen Fold Belt and adjacent parts of Central Ellesmere Fold Belt, Ellesmere Island. Geological Survey of Canada Bulletin, 430: 248.

Vermeesch, P. (2021). Maximum depositional age estimation revisited. *Geoscience Frontiers*, 12(2): pp. 843-850. DOI: 10.1016/j.gsf.2020.08.008

Vermeesch, P. (2020). Unifying the U–Pb and Th–Pb methods: joint isochron regression and common Pb correction. *Geochronology*, 2(1): pp. 119-131. DOI: 10.5194/gchron-2-119-2020

Vermeesch, P. (2004). How many grains are needed for a provenance study?. *Earth and Planetary Science Letters*, 224(3/4): pp. 441-451. DOI: 10.1016/j.epsl.2004.05.037

Wiedenbeck, M., Hanchar, J.M., Peck, W.H., Sylvester, P., Valley, J., Whitehouse, M.J., Kronz, A., Morishita, Y., Nasdala, L., Fiebig, J., Franchi, I., Girard, J.P., Greenwood, R.C., Hinton, R., Kita, N., Mason, P.R.D., Norman, M., Ogasawara, M., Piccoli, P.M., Rhede, D., Satoh, H., Schulz-Dobrick, B., Skar, O., Spicuzza, M.J., Terada, K., Tindle, A., Togashi, S., Vennemann, T., Xie, Q., Zheng, Y.F. (2004). Further characterization of the 91500 zircon crystal. *Geostandards and Geoanalytical Research*, 28(1): pp. 9-39. DOI: 10.1111/j.1751-908X.2004.tb01041.x

Whitehouse, M.J., Kamber, B.S. (2005). Assigning dates to thin gneissic veins in high-grade metamorphic terranes: a cautionary tale from Akilia, Southwest Greenland. *Journal of Petrology*, 46(2): pp. 291-318. DOI: 10.1093/petrology/egh075

Whitehouse, M.J., Kamber B.S., Moorbath, S. (1999). Age significance of U–Th–Pb zircon data from early Archean rocks of west Greenland – a reassessment based on combined ion microprobe and imaging studies. *Chemical Geology*, 160(3): pp. 210-224. DOI: 10.1016/S0009-2541(99)00066-2

White, W.M. (2015). *Isotope Geochemistry*. 1st ed. Chichester, West Sussex: John Wiley & Sons. ISBN 978-0-470-65670-9.

Zheng, D., Wu, S., Ma, C., Xiang, L., Hou, L., Chen, A., Hou, M. (2022) Zircon classification from cathodoluminescence images using deep learning. *Geoscience Frontiers*, 13(6):101436, 2022. DOI: 10.1016/j.gsf.2022.101436.

Appendix A - Mineral Abbreviations

Table 2: Mineral abbreviations

MINERAL	ABBREVIATION
Actinolite	Act
Amphibole	Amp
Biotite	Bt
Calcite	Cal
Chlorite	Chl
Clinopyroxene	Cpx
Epidote	Ep
Opakes	Opq
Quartz	Qz
Lithic fragments	Lit
White mica	Wm

Appendix B: Petrographic descriptions

VP17-26b

Descriptions based on hand sample

The hand sample was not available.

Descriptions based on thin section

Mineral composition

Primary phase of plagioclase (54%), amphibole (6%), unidentified opaque oxides (7%), calcite (3 %), quartz (1%), and groundmass (23%). Secondary phase of chlorite (7%) and fine-grained white mica.

The sample exhibits a porphyritic texture characterized by a dominant phenocrystic phase of plagioclase, pseudomorph amphibole, opaque oxides, and minor calcite set within finer groundmass. Plagioclase is present as subhedral to anhedral crystals with some tabular and elongated forms. Many grains exhibit polysynthetic and simple twinning, as well as growth zonation (oscillatory zoning in some cases). Some of the plagioclases exhibit embayment's along their edges and sieve textures, indicative of magmatic resorption and disequilibrium conditions during their formation. The plagioclases are commonly sericitized, especially towards the crystal cores. Som plagioclases are however entirely replaced by fine-grained white mica, preserving only a pseudomorph outline of their primary crystal shape. Amphibole

is no longer preserved in its original form but appears as pseudomorphs replaced by fibrous chlorite, which exhibits anomalous blue birefringence in XPL and a pale green to brown color in PPL. Nonetheless, the original crystal habits and the diagnostic 60°/120° cleavage angles are locally retained in the amphibole. There is a minor phase of calcite present as a few larger phenocrysts or as fine-grained masses, exhibiting rhombohedral twinning and high fourth-order birefringence, often accompanied by inclusions of opaque oxides.

The groundmass comprises microlitic plagioclase, fine-grained amphibole, quartz, and scattered opaque oxides. It displays a brown, grainy texture in PPL, consistent with low-temperature alteration, likely to clay minerals or cryptocrystalline sericite. Collectively, the mineral assemblage and alteration textures suggest that this sample originated as an intermediate to mafic porphyritic rock of basaltic composition and subsequently underwent hydrothermal alteration under sub-greenschist to greenschist facies conditions.

VP17-27

Descriptions based on hand sample

The sample is a medium- to coarse-grained plutonic mafic rock characterized by interlocking plagioclase and pyroxene. There is a minor phase of chlorite associated with the pyroxene. The pyroxene is shifting from a dark green to black in color.

Descriptions based on thin section

Mineral composition

Primary phase of plagioclase (55%), clinopyroxene (32%), and accessory unidentified opaque oxides (<1%). A secondary phase of chlorite (10%), actinolite (3%), and fine-grained white mica.

The sample is characterized by an abundance of plagioclase in various sizes and shapes, ranging from medium-sized euhedral and tabular to coarse anhedral grains. Many plagioclases display polysynthetic and simple twinning, as well as compositional zoning, though signs of late-stage magmatic resorption are common, evident through embayed and corroded grain margins. Many of the plagioclase exhibit a secondary alteration phase, where some grains are extensively sericitized, preserving only pseudomorph outlines of the primary phase, while others remain relatively intact with only limited alteration at the center of the crystal. Clinopyroxene is present as subhedral to anhedral crystals and numerous grains show

exsolution lamellae, suggesting magmatic unmixing during cooling, while others display partial resorption, typically along a single crystal face, which is frequently replaced by fine-grained chlorite. A thin rim of actinolite is locally developed on some clinopyroxenes. Chlorite occurs as fine-grained aggregates, altering both clinopyroxene and plagioclase, and is distinguished by its pale green color in PPL and anomalous high birefringence of blue to green interference colors in XPL. Several thin fractures traverse the sample, filled with white mica and fine-grained pyroxene, from which zones of sericitization and chloritization extend outward, marking pathways of fluid-assisted alteration. The overall texture and mineralogy suggest a protolithic gabbroic rock, that has undergone moderate to strong hydrothermal alteration, particularly along fracture networks.

VP17-29

Descriptions based on hand sample

The sample is a fine-to-medium-grained mafic volcanic rock. Elongated, lath-shaped plagioclase can be observed, as well as elongated pyroxene. There is a minor phase of dark oxides and a few clusters of pale-colored calcite.

Descriptions based on thin section

Mineral composition

A primary phase of plagioclase (50%), clinopyroxene (14%), calcite (15%), unidentified opaque oxides (6%), and accessory biotite (1%). A secondary phase of chlorite (10%), actinolite (3%), epidote (1%), and fine-grained white mica.

The sample is characterized by an intergranular texture with abundant plagioclase in various sizes, primarily as fine-grained, elongated, tabular to lath-shaped grains. The plagioclases commonly show polysynthetic and simple twinning, as well as compositional zoning. Several larger plagioclase crystals exhibit resorbed edges and sieve textures, indicative of magmatic disequilibrium and late-stage partial resorption. Sericitization is pervasive throughout the plagioclase population, with many grains replaced wholly or partially by fine-grained white mica. Clinopyroxene occurs as subhedral to anhedral, elongate grains with irregular and often embayed margins, many of which are altered along their rims by fibrous chlorite and actinolite. In some cases, clinopyroxene is completely pseudomorphed by secondary chlorite minerals, preserving only its crystal outline. Calcite appears in anhedral clusters displaying its characteristic rhombohedral twinning and fourth-order birefringence. The calcites are commonly embayed and spatially associated with secondary chlorite, suggesting a potential

alteration relationship. Chlorite occurs as fibrous masses surrounding calcite and clinopyroxene, as well as interstitially between other minerals. Actinolite is present as fibrous rim replacements of clinopyroxene, and minor epidote is occasionally found near chlorite clusters. Accessory phases include opaque oxide minerals and sparse biotite.

The widespread development of chlorite, actinolite, fine-grained white mica, and minor epidote reflects a secondary alteration assemblage consistent with greenschist-facies metamorphism or hydrothermal overprint involving a hydrous phase. The association of calcite with chloritized pyroxene may further suggest fluid-mediated carbonate alteration during retrogression. The overall texture and mineralogy suggest an originally basaltic rock with a carbonate component, which has undergone moderate to strong secondary alteration.

VP17-30

Descriptions based on hand sample

The sample is a fine-to-medium-grained mafic plutonic rock. Plagioclase is visible with the naked eye in a variety of shapes, from anhedral to euhedral and tabular. Some plagioclases exhibit an altered green color, possibly due to the presence of chlorite, while others are paler white in color. Dark green to black pyroxene can also be observed with a hand lens.

Descriptions based on thin section

Mineral composition

A primary phase of plagioclase (50%), clinopyroxene (23%), hornblende (6%), unidentified opaques (6%), and biotite (1%). A secondary phase of chlorite (9%), actinolite (3%), epidote (2%) and fine-grained white mica.

The sample displays an intergranular to subophitic texture, characterized by abundant medium-sized plagioclase occurring as subrounded, tabular grains that interlock to form the primary framework of the sample. The plagioclases commonly exhibit polysynthetic twinning and compositional zoning. Sericitization is widespread, particularly concentrated toward the centers of grains; in more altered cases, plagioclase is nearly or entirely replaced by fine-grained white mica, preserving only its external shape. Clinopyroxene is present in a range of sizes, typically as subrounded grains that display simple twinning and frequent resorption textures. Extensive chloritization is evident along embayed grain boundaries of the clinopyroxens, suggesting interaction with hydrothermal fluids. In several cases,

clinopyroxenes also exhibit a thin reaction rim of fibrous actinolite. Hornblende occurs as anhedral to euhedral crystals, some of which form single grains and some that form coronas around the clinopyroxenes, implying a late-magmatic or subsolidus reaction. Some of the hornblende crystals also show alteration by secondary chlorite. Accessory biotite is also observed, although it is frequently replaced by chlorite. Epidote occurs as minor, subrounded grains, identifiable by its high birefringence or the third-order interference color in XPL as well as its basal cleavage. Lastly, opaque oxide minerals are disseminated throughout the matrix.

The secondary mineral assemblage includes chlorite, actinolite, epidote, and fine-grained sericite, reflecting alteration under greenschist-facies conditions. The coexistence of hornblende coronas as well as widespread secondary chloritization and actinolite alteration indicates a magmatic-to-subsolidus transition that was overprinted by greenschist facies and fluid-driven metamorphic alteration. The overall textures and mineralogy indicate a protolithic gabbroic rock that has undergone secondary alteration.

VP17-34

Descriptions based on hand sample

The sample is a fine-to-medium-grained mafic volcanic rock. Tabular plagioclase can be observed with the naked eye. In some of the larger plagioclases, compositional zoning is observed, characterized by a darker core and a lighter rim relationship. Dark green to black pyroxene can also be observed, and a minor portion of chlorite is associated with the plagioclases and at the rim of the pyroxene.

Descriptions based on thin section

Mineral composition

A primary phase of plagioclase (49%), clinopyroxene (29%), unidentified opaque oxides (5%), and biotite (2%). A secondary phase of chlorite (10%), actinolite (4%), epidote (1%), and fine-grained white mica.

The sample exhibits an intergranular texture, characterized by fine to medium-sized plagioclase grains. The plagioclases occur in a variety of forms, ranging from anhedral to euhedral and tabularly formed. Many of them exhibit growth zoning and commonly display polysynthetic and simple twinning, but embayments and resorbed grain margins are widespread, with occasional sieve textures indicating disequilibrium during crystallization.

Most plagioclases exhibit secondary sericitization, particularly concentrated toward grain centers. Some plagioclases also show partial chloritization along resorbed faces.

Clinopyroxene is present as subrounded grains, many of which exhibit resorbed margins, embayments, and irregular outlines. Simple twinning is common, and some grains possess thin reaction rims of fibrous actinolite. Chlorite occurs both as fibrous interstitial masses and as replacement rims or patches affecting clinopyroxene, plagioclase, and biotite. Accessory epidote is observed as small, anhedral, rounded grains with high birefringence. Opaque minerals are dispersed throughout the matrix.

The secondary mineral assemblage of chlorite, actinolite, fine-grained white micas, and epidote indicates pervasive greenschist-facies alteration or a hydrous alteration phase. The widespread resorption textures suggest post-magmatic fluid interaction and recrystallization under subsolidus conditions. The overall textures and mineralogy indicate a protolithic basaltic rock that has undergone secondary alteration.

VP17-38

Descriptions based on hand sample

The sample is a medium-to coarse-grained plutonic mafic rock. Plagioclase crystals can be observed with the naked eye, and they are present as subhedral to more euhedral tabular shapes. There is one type of reddish-brown iron oxide present that exhibits weathered textures. Dark to green tinter pyroxene can also be observed.

Descriptions based on thin section

Mineral composition

A primary phase of plagioclase (55%), clinopyroxene (18%), unidentified opaque oxides (8%), and accessory biotite (1%). A secondary phase of chlorite (14%), hornblende (2%), actinolite (1%), epidote (1%), and fine-grained white mica.

The sample is a medium- to coarse-grained, equigranular gabbroic rock characterized by subhedral to euhedral, tabularly formed plagioclase laths that interlock with anhedral to subhedral clinopyroxenes. The plagioclase displays polysynthetic twinning and broad bands of growth zoning; however, many grains exhibit embayments's and partially resorbed margins. Clinopyroxene occurs as pale green to colorless, subrounded patches. Many of them are locally zoned but several grains exhibit embayed and partially resorbed edges. Sparse hornblende also appears as coronas around the clinopyroxene, indicating a late-stage

disequilibrium magmatic reaction. There is a minor phase of disseminated opaque oxides in close association with the clinopyroxene. Biotite occurs as an accessory phase exhibiting a platy morphology and partial replacement by secondary chlorite along its cleavage planes.

The sample appears to have undergone extensive alteration by a secondary alteration phase. Some plagioclases are completely pseudomorphed by fine-grained white mica, retaining only the primary crystal outline, while others have limited alteration, mainly at the center of the grain. Clinopyroxene also exhibits alteration, mostly along its embayed edges, where subsequent fibrous chlorite alters the grain, but some grains are entirely consumed by chlorite. Some of the clinopyroxenes have thin reaction rims of pale green actinolite (distinguished from chlorite by lower birefringence, 120/60° cleavage, and weaker pleochroism). Chlorite also replaces plagioclase along embayed and resorbed margins and additionally forms interstitial fibrous mats between other grains. Epidote is also present as minor anhedral masses within sericitized zones.

The sericite-chlorite-actinolite-epidote alteration assemblage, combined with widespread pseudomorphous replacement of plagioclase and clinopyroxene, reflects a greenschist-facies hydration event that overprinted the original gabbroic protolith under metamorphic or hydrothermal conditions.

VP17-44

Descriptions based on hand sample:

The sample is a medium to coarse-grained plutonic mafic rock. It is composed of subhedral to euhedral and tabular-formed plagioclases that are green-tinted to light grey in color. Pyroxene is also present, ranging from black to dark green in colors. Minor fibrous chlorite can be observed associated with the pyroxenes.

Descriptions based on thin section:

Mineral composition

A primary phase of plagioclase (53%), clinopyroxene (20%), unidentified opaque oxides (10%), accessory biotite (3%), and calcite (1%). A secondary phase of chlorite (9%), green amphibole (2%), epidote (2%), and fine-grained white mica.

The sample is a medium- to coarse-grained phaneritic gabbroic rock characterized by abundant subhedral to euhedral and tabular plagioclase laths. The plagioclase commonly

exhibits polysynthetic twinning and broad growth zoning bands, but many grains are embayed or have corroded grain boundaries. Clinopyroxene occurs as pale green to colorless, subrounded prisms with locally resorbed margins; low-order interference colors indicate a relatively calcic composition. Two types of opaque oxides are present: one reddish-brown (PPL) oxide associated with secondary chlorite aggregates, and one extinct (XPL/PPL), featureless grains disseminated in the sample. Sparse biotite appears along pyroxene grain boundaries, locally altered by chlorite.

There is evidence of a secondary alteration phase. Plagioclase is extensively sericitized, mainly at the center of the grains, but some grains are entirely replaced by fine-grained white mica. Chlorite replaces plagioclase along embayments and forms fibrous mats that pseudomorph clinopyroxene as well. Many of the clinopyroxenes also have thin fibrous reaction rims of actinolite. Additional chlorite rims surround some of the biotite grains, suggesting Fe-Mg mobilization. Accessory epidote occurs as anhedral masses within the altered zones. The white mica, chlorite, actinolite and epidote assemblage is characteristic of a greenschist-facies, or a hydration event superimposed on the gabbroic protolith.

VP17-45

Descriptions based on hand sample:

The sample has a general cryptocrystalline texture with a mafic composition. A hand lens reveals a few elongated lath-shaped plagioclase microphenocrysts. The groundmass appears to be primarily composed of dark clinopyroxene and plagioclase. Flow bands can also be identified, indicating the direction of flow during crystallization.

Descriptions based on thin section:

A few mineral phases could be identified in the thin section, but due to the cryptocrystalline texture, no modal mineralogy could be estimated.

The sample has vitric groundmass, indicating an extremely fast cooling rate. Well-developed flow banding appears as curving, alternating bands of lighter and darker composition, indicative of high-viscosity lava that has undergone laminar flow before cooling. Angular glass shards are also present, and some of them appear slightly welded along their edges, suggesting incipient welding. Small, elongated, lath-shaped plagioclases exhibit polysynthetic twinning. There are a few rounded quartz grains that were identified by their

undulous extinction and lack of cleavage. A minor phase of two different oxide minerals is present as anhedral, disseminated masses, one of which exhibits reddish-brown colors in PPL and XPL, while the other is extinct in both PPL and XPL.

There are lenticular areas of replaced plagioclase, now altered by fine-grained fibrous chlorite and white mica. These areas exhibit a pale green color in PPL with a high birefringence of a bluish tint (XPL), indicative of chlorite. Some parts showed dusty fine-grained zones, characteristic of sericitization. Devitrification can also be observed in the groundmass, indicating an initial phase of amorphous glass that are breaking down into fine-grained crystalline material, which at present locally hosts fine quartz ± feldspar microlites, resulting in a dusty birefringence (XPL). In PPL, devitrified zones exhibit a slightly brownish tint, a common characteristic associated with secondary hydration or greenschist facies metamorphism. The overall textures and mineralogy indicate an cryptocrystalline mafic lava that has undergone secondary alteration.

VP17-56

Descriptions based on hand sample:

The sample is a medium to coarse-grained phaneritic mafic rock. It is characterized by abundant subhedral to euhedral and tabular plagioclases, as well as black to dark green pyroxene. Some plagioclases have a green tint, while others range from white to grey in color. Growth zoning can be observed in some of the larger plagioclases, characterized by a darker core and a whiter rim. A minor phase of iron oxides is present as a cluster of disassembled reddish-brown clusters.

Descriptions based on thin section:

Mineral composition

A primary phase of plagioclase (54%), clinopyroxene (20 %), unidentified opaque oxides (9%), and accessory biotite (1%). A secondary phase of chlorite (13%), actinolite (3%), epidote (2 %), and fine-grained white mica.

The sample exhibits an intergranular texture, dominated by plagioclase and clinopyroxene, with disseminated opaque oxides and minor biotite. Plagioclase occurs as subhedral to more euhedral and tabular laths. Most plagioclases exhibit well-developed polysynthetic twins and, in some cases, broad compositional zoning. Several plagioclase grains show one or more corroded crystal faces, indicating late-stage resorption. Clinopyroxene occupies intercumulus

pockets and narrow oikocrystic patches around plagioclase laths. The clinopyroxenes are pale beige to colorless in PPL and exhibit low-order interference colors in XPL, consistent with a comparatively calcic composition rather than iron-rich. Many of the clinopyroxenes exhibit irregular or saw-toothed grain boundaries, locally enclosing some of the plagioclase. Opaque oxides form anhedral clusters. Accessory biotite appears as sparse, platy-grained, extensively altered by secondary chlorite.

There is evidence of a secondary alteration phase where the plagioclases exhibit variable degrees of sericitization. Most plagioclases exhibit alteration limited to the core of the grain, while others are extensively altered and wholly replaced by fine-grained white mica.

Clinopyroxene is locally replaced along fractures and embayed edges by fine-grained, fibrous chlorite, and is commonly rimmed by needle-shaped actinolite; in a few cases, the original primary phase of clinopyroxene is almost entirely pseudomorphed by chlorite aggregates. Chlorite also replaces plagioclase and biotite, and forms interstitial fibrous mats between larger grains. Accessory epidote occurs as scattered anhedral clusters within altered zones. The assemblage of fine-grained white mica, chlorite, actinolite, epidote is indicative of a greenschist-facies metamorphic overprint or possibly a hydrous phase, superimposed on an otherwise well-preserved gabbroic protolith.

VP17-66

Descriptions based on hand sample:

Hand sample not available.

Descriptions based on thin section

Mineral composition:

Due to the samples' aphanitic and welded texture, it is difficult to identify every single mineral phase; therefore, no modal abundance was estimated.

The sample displays a fine-grained reworked lithic-crystal tuff with a fragmental texture. The sample is poorly sorted, containing angular to subrounded plagioclase grains, with some elongated latch-shaped ones. In some of the larger plagioclases, polysynthetic twinning is observable. A minor phase of one or several types of oxides is present, being extinct in both PPL and XPL. There are also rounded quartz grains exhibiting undulous extinction, and volcanic lithic fragments are identified by their mixed composition and complex internal

textures, indicating a mixed source. A few small, rounded zircon grains can also be observed, exhibiting high birefringence with a fourth-order interference color and high relief, which makes them stand out sharply compared to the surrounding minerals. The matrix appears to be fine-grained or devitrified volcanic glass, composed of a pale green to brown mineral with low birefringence, possibly altered by chlorite or another clay mineral. The presence of fragmental grains and volcanic debris embedded in a fine, possibly altered groundmass supports the interpretation of a moderately altered and reworked tuffaceous rock.